

1 **Assessment of the vulnerability of buildings destroyed during**
2 **postfire debris flow events in Kule village, Yajiang County, China**

3

4 **Author names:**

5 **Jinshui Wang¹², Jiangang Chen^{123*}, Lu Zeng¹², Fei Yang¹², Xiao Li¹², Wanyu**
6 **Zhao¹²³, Huayong Chen¹²**

7

8 **Affiliations**

9 ¹State Key Laboratory of Natural Hazards and Engineering Safety, Institute of Mountain
10 Hazards and Environment, Chinese Academy of Sciences, Chengdu, 610299, China;

11 ²University of Chinese Academy of Sciences, Beijing, 100049, China.

12 ³Sichuan Province Engineering Technology Research Center of Mountain Hazards, Chengdu,
13 610299, China.

14

15 **Corresponding author**

16 Jiangang Chen*

17 Email: chenjg@imde.ac.cn

18

19 **Abstract**

20 Debris flows are frequently triggered by rainstorms after wildfires and pose severe threats
21 to downstream residents and buildings in mountainous regions. However, there has been limited
22 focus on developing a comprehensive framework to assess the physical vulnerability of
23 buildings to postfire debris flows. This study presents a quantitative approach for establishing
24 a physical vulnerability model based on observed building damage and simulated debris flow
25 intensities. Detailed field surveys established a building damage database in Kule village,
26 Yajiang County. Numerical simulations using the FLO-2D model were performed to reproduce
27 the debris flow process and quantify the debris flow intensity, including the flow depth, flow
28 velocity, impact pressure, momentum flux, overturning moment, and relative burial height.
29 Physical vulnerability curves were developed for brick-concrete buildings and compared with
30 those obtained in previous studies, and the differences in vulnerability curves, intensity
31 indicators, and functional models were examined. The results revealed that the lognormal
32 cumulative distribution function (LNCDF) model achieved the best performance, with relative
33 error less than 10% and prediction accuracy exceeding 85%. Critical thresholds for complete
34 building damage were identified as a flow depth of 2.5 m and impact pressure of 25 kPa. The
35 momentum flux demonstrated greater sensitivity in distinguishing different damage categories,
36 whereas the impact pressure provided more precise vulnerability index predictions. The
37 proposed physical vulnerability model can evaluate the building structural resistance to debris
38 flows in wildfire-affected areas, providing a systematic foundation for risk management and
39 mitigation strategies.

40 **Keywords:** Postfire debris flow, Vulnerability, Building damage, Emergency evacuation

41 **1. Introduction**

42 Debris flows are recurring and destructive hazards in mountainous regions, posing
43 significant threat to downstream buildings and human lives (Cui et al., 2018; Chen et al., 2021).
44 Recently, debris flow disasters after wildfires have received widespread attention, as wildfires
45 increase debris flow susceptibility by reducing vegetation cover, altering soil hydrology, and
46 lowering rainfall thresholds for initiation (Kean et al., 2019; Thomas et al., 2023; Ouyang et al.,
47 2023). These effects can persist for years and generate larger events compared to unburned
48 conditions, amplifying risks to downstream communities (Gorr et al., 2023; Vahedifard et al.,
49 2024). Destructive postfire debris flow events such as the 2018 Montecito, California disaster
50 (23 fatalities, >400 buildings damaged), the 2021 Muli County, China event (186 houses
51 destroyed), and the 2024 Yajiang County, China event highlight the urgent need for
52 vulnerability assessment (Kean et al., 2019; Ouyang et al., 2023; He et al., 2024). However, a
53 comprehensive framework for assessing physical vulnerability of buildings to postfire debris
54 flows remain limited.

55 Assessing building vulnerability to debris flows is essential for risk assessment, emergency
56 evacuation, disaster reduction and rural planning (Eidsvig et al., 2014; Zhang et al., 2018; Wang
57 et al., 2024). Physical vulnerability is defined as the expected degree of loss to structures under
58 a given hazard intensity (Fuchs et al., 2007; Papathoma-Köhle et al., 2021). Over the past two
59 decades, building vulnerability assessments have transitioned from qualitative approaches to
60 quantitative methods, specifically data-driven and mechanism-based models (Luo et al., 2023).

61 These methods are commonly represented through three primary tools for debris flow
62 vulnerability: matrices, indicators, and curves (Papathoma-Köhle et al., 2017). Among these
63 methods, vulnerability curves are widely employed to quantify the relationship between the
64 debris flow intensity and the extent of building damage (Zhang et al., 2018; Luo et al., 2020).
65 With increasing hazard intensity, the degree of damage follows a monotonically increasing
66 curve (Lee et al., 2024), ranging in value from 0 (no damage) to 1 (complete damage), as
67 determined via the data-driven approach. Several statistical method-based studies have been
68 conducted to develop physical vulnerability curves for debris flows on the basis of field data
69 (Lee et al., 2024). They have established curves based on intensity-damage relationships (Fuchs
70 et al., 2007; Totschnig et al., 2011) for specific regions and building types like brick–concrete
71 (BC) and reinforced concrete (RC) structures (Kang and Kim, 2016).

72 However, in many regions, the availability of debris flow data is often limited because of
73 the infrequent occurrence of significant debris flow events (Navratil et al., 2013; Wang et al.,
74 2024). Moreover, although valuable debris flow intensity-related data are regularly collected
75 (Marchi et al., 2002), few studies have focused on monitoring the impact of debris flows on
76 buildings (Jakob et al., 2012). Therefore, dynamic numerical models have increasingly been
77 employed to reconstruct debris flow processes and determine the hazard intensity (Zhang et al.,
78 2018; Ouyang et al., 2019; Chang et al. 2020). Such runout models play a critical role in
79 bridging data gaps (Chen et al., 2021) and can serve as inputs for vulnerability functions to
80 predict building damage (Barnhart et al., 2024). In prior studies, different numerical simulation
81 models have been used to develop vulnerability curves and evaluate building damage (Luo et

82 al., 2023), including Flow-R, RAMMS, FLO-2D, and D-Claw (Lee et al., 2024; Barnhart et al.,
83 2024). One of the most frequently used models is FLO-2D, a depth-integrated continuum
84 method and volume-conservation model capable of simulating non-Newtonian flows (Wang et
85 al., 2024; Wei et al., 2024), which has been widely utilized in debris flow simulations (Quan
86 Luna et al., 2011; Zhang et al., 2018; Chen et al., 2021; Wang et al., 2024). Previous studies
87 using FLO-2D have developed vulnerability curves for multiple intensity indicators, including
88 flow depth, velocity, impact pressure, momentum flux, overturning moment, and relative burial
89 height, across different building types such as brick-concrete, reinforced concrete, and masonry
90 structures. Notably, the accuracy of this numerical model highly depends on the selection of
91 parameter values (Chen et al., 2021), which requires a comprehensive understanding of debris
92 flow properties, including their formation mechanisms, frequency, and intensity (Chang et al.,
93 2020). Furthermore, accurately calculating the debris flow volume (Barnhart et al., 2024) and
94 the peak discharge (Wang et al., 2024) is critical for ensuring the reliability of runoff dynamics
95 prediction outcomes.

96 In addition, the uncertainty and accuracy of vulnerability curves are affected not only by
97 the adopted numerical model but also by the debris flow intensity and building damage
98 attributes, as well as the statistical functional models linking the two (Luo et al., 2023; Lee et
99 al., 2024). First, there are numerous intensity indicators, including the two easily obtained direct
100 parameters of the flow depth and velocity (Eidsvig et al., 2014; Kang and Kim, 2016;), as well
101 as derivative parameters, such as the impact pressure (Quan Luna et al., 2011; Lee et al., 2024;
102 Wang et al., 2024), momentum flux (Jakob et al., 2012; Ouyang et al., 2019; Chen et al., 2021;

103 Barnhart et al., 2024), overturning moment (Zhang et al., 2018), and relative burial height
104 (Totschnig et al., 2011; Zhang et al., 2018). Second, various factors related to buildings can
105 significantly influence vulnerability assessments, including building features such as the
106 number of floors, direction, shielding effects and construction codes (Luo et al., 2020), as well
107 as the building structure type such as wood-frame buildings, masonry buildings, BC buildings,
108 and RC buildings, which have been studied extensively (Lee et al., 2024). Additionally, building
109 damage due to debris flows has been primarily classified qualitatively (Hu et al., 2012). Within
110 this framework, the damage state is commonly categorized as slight, moderate, extensive, and
111 complete damage (Luo et al., 2023). Third, vulnerability curves can be fitted using several
112 functional models (Luo et al., 2023), such as polynomial functions, logistic functions, Weibull
113 distributions, exponential functions, lognormal cumulative distribution function (LNCDF) and
114 Avrami functions (Fuchs et al. 2007; Quan Luna et al., 2011; Eidsvig et al., 2014; Luo et al.,
115 2023; Lee et al., 2024). Thus, further research remains needed to determine the most reliable
116 predictions on the basis of different vulnerability functions and hazard intensity measures.

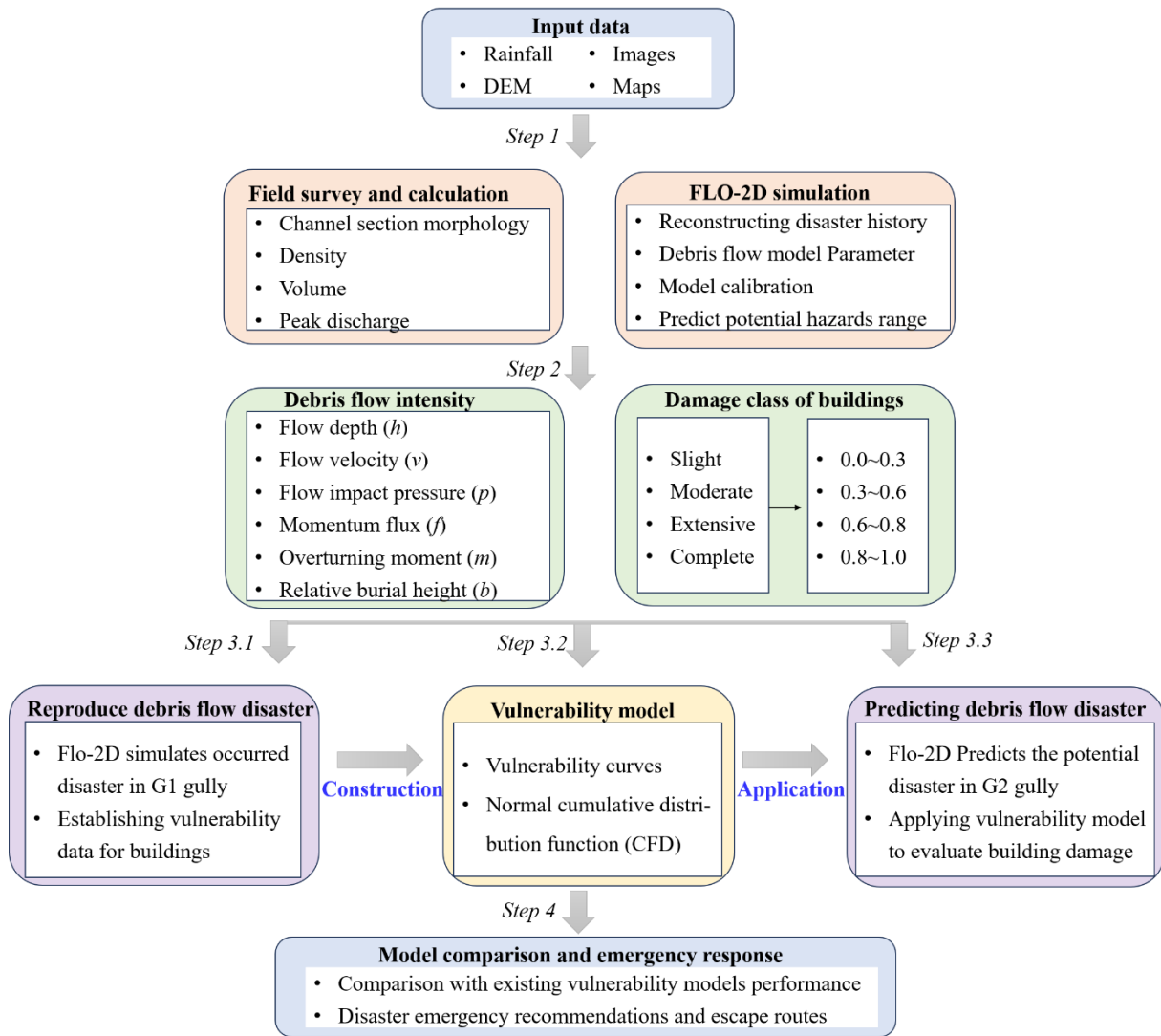
117 In this study, the aim was to comprehensively assess the physical vulnerability of buildings
118 damaged during postfire debris flows in Kule village, Yajiang County. The primary objectives
119 are as follows: (1) To analyze the characteristics of postfire debris flows and establish a building
120 damage database through field investigations. (2) To reconstruct debris flow events via FLO-2D
121 numerical simulations in order to determine debris flow intensity. (3) To develop physical
122 vulnerability curves for BC buildings for assessing the establishment and application of a
123 vulnerability assessment model. (4) To compare the differences in performance among various

124 vulnerability approaches, such as existing intensity indicators, curves, and function models.
125 This work aims to provide insights for advancing postfire debris flow assessments, improving
126 vulnerability models, and guiding emergency evacuation efforts in this region.

127 **2. Methods**

128 The methodological procedure in this study is divided into four steps (Fig. 1). In step 1,
129 we conducted a field investigation and obtained images of burned areas, channel morphology,
130 grain size distribution, and features of buildings in gullies affected by debris flows (Fig. 4).
131 Then, we calculated the physical characteristic parameters of postfire debris flows. Finally, we
132 reproduced and predicted dynamic runout processes via numerical simulations using the FLO-
133 2D model. In step 2, we employed a numerical model to calculate six indicators of the debris
134 flow intensity (Zhang et al., 2018). Moreover, the damage degree of buildings was classified,
135 and vulnerability index values were assigned on the basis of the degree of damage to buildings
136 (Wang et al., 2024). In step 3, we established building vulnerability curves and a function model
137 using the reconstructed debris flow intensity and building damage information from the G1
138 gully (after postfire debris flow occurrence). We subsequently applied the vulnerability model
139 to predict potential future scenarios of building damage in the G2 gully (under potential future
140 debris flow scenarios), aiming to assess the compound, bilateral threat that both gullies pose to
141 the downstream Kule Village community. Finally, in step 4, we verified and compared the
142 performance of the proposed vulnerability model with that of previous models and provide
143 suggestions for emergency response and evacuation routes during disasters in Kule village. This
144 methodology facilitates a comprehensive analysis of the potential effects of future postfire

145 debris flow events on buildings within the region, offering valuable insights for formulating
 146 disaster management and mitigation strategies.



147

148

Figure 1. Methodological framework

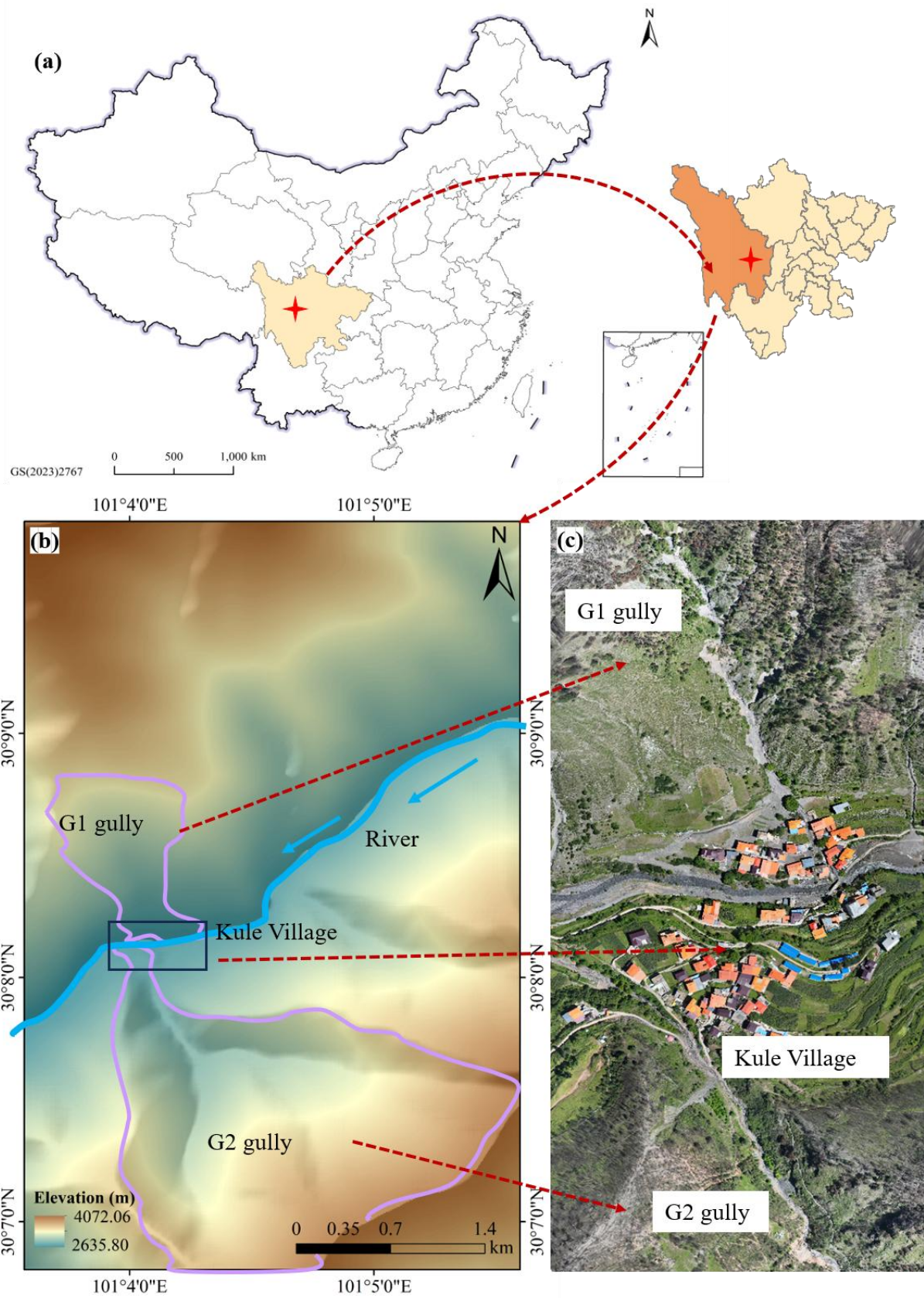
149 **2.1. Field investigation and data acquisition**

150 **2.1.1 Study area**

151 The study area is located in Yajiang County, Sichuan Province, China. Yajiang County
 152 occurs in the southeastern part of the Qinghai–Tibet Plateau and the central segment of the
 153 Hengduan Mountains within the basin of the Yalong River (He et al., 2024). The Kule watershed

154 (coordinates: 101°4'12.53" E, 30°7'55.88" N) is located in the northeastern part of Xiala town
155 in Yajiang County, and the terrain encompasses mainly high mountains and deep canyons. The
156 study area of the Kule watershed contains two primary gullies (G1 and G2), which converge
157 with the main river in the downstream impact area of Kule village (Fig. 2). Kule village contains
158 58 households with 308 people, and the Kule River flows through the downstream alluvial fan
159 of this village. The left and right banks of the village are impacted by the G1 and G2 gullies,
160 respectively. The catchments of the G1 gully and G2 gully cover areas of 1.4 and 3.5 km²,
161 respectively, and the terrain elevation differences range from 850~1,015 m. Geologically, the
162 area primarily comprises Late Triassic silty slate. The bedrock is severely weathered and
163 structurally fragmented. Within the catchment, the bedrock is overlain by Quaternary sediments
164 that are approximately 1.0~3.0 m thick (He et al., 2024). The thin residual soil layer is
165 susceptible to failure during periods of intense rainfall.

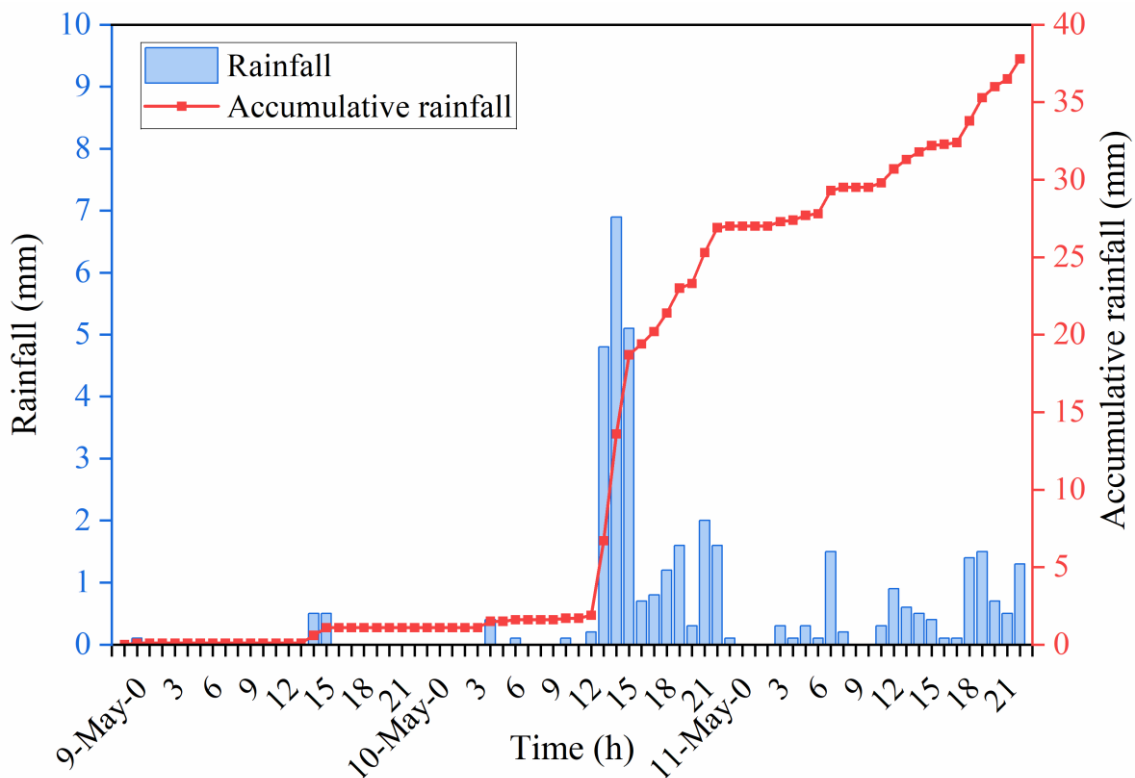
166 On 15 March, 2024, a wildfire ignited in Yajiang County, burning 278.8 km² of
167 mountainous forest and affecting 250 watersheds, with moderate-high burn levels accounting
168 for more than 50% of the total catchment area (He et al., 2024). Several postfire debris flows
169 occurred in the burned catchments on May 10 that were induced by rainfall events following
170 the fire. In particular, the postfire debris flows in the G1 gully in Kule village destroyed 36
171 houses, blocked roads, and displaced people. Postfire debris flow and building damage data
172 were collected from this event to support building vulnerability assessment and disaster
173 reduction efforts (Zhang et al., 2018; Gorr et al., 2023).



174

175 Figure 2. Location of the study area in the Kule Gully, Yajiang County, Sichuan Province, China.

176 Yajiang County occurs in a plateau monsoon climate zone, and the long-term annual
 177 precipitation ranges from 600 to 1200 mm, with precipitation mainly concentrated from June
 178 to September, which accounts for about 86% of the annual total, with a recent decadal average
 179 (2010–2020) of 705 mm. The rainstorm started at 14:00 on 10 May and lasted until 11 May,
 180 according to records from a rainfall monitoring station (coordinates: 101°1'20" E, 30°1'57" N).
 181 The maximum recorded hourly rainfall intensity was 6.9 mm/h, and the accumulated rainfall
 182 reached 37.8 mm (Fig. 3). Notably, the rainfall threshold of postfire debris flows is much lower
 183 than that of nonfire debris flows (Ouyang et al., 2023). In particular, low-intensity rainfall can
 184 trigger postfire debris flows in the G1 gully, and the G2 gully occurs in a state in which debris
 185 flows can occur at any time. Owing to wildfires, a large amount of loose material remains on
 186 hillslopes and in channels, which can provide abundant material sources for triggering debris
 187 flows (McGuire et al., 2024). Thus, debris flow activity in the G1 and G2 gullies may last longer.

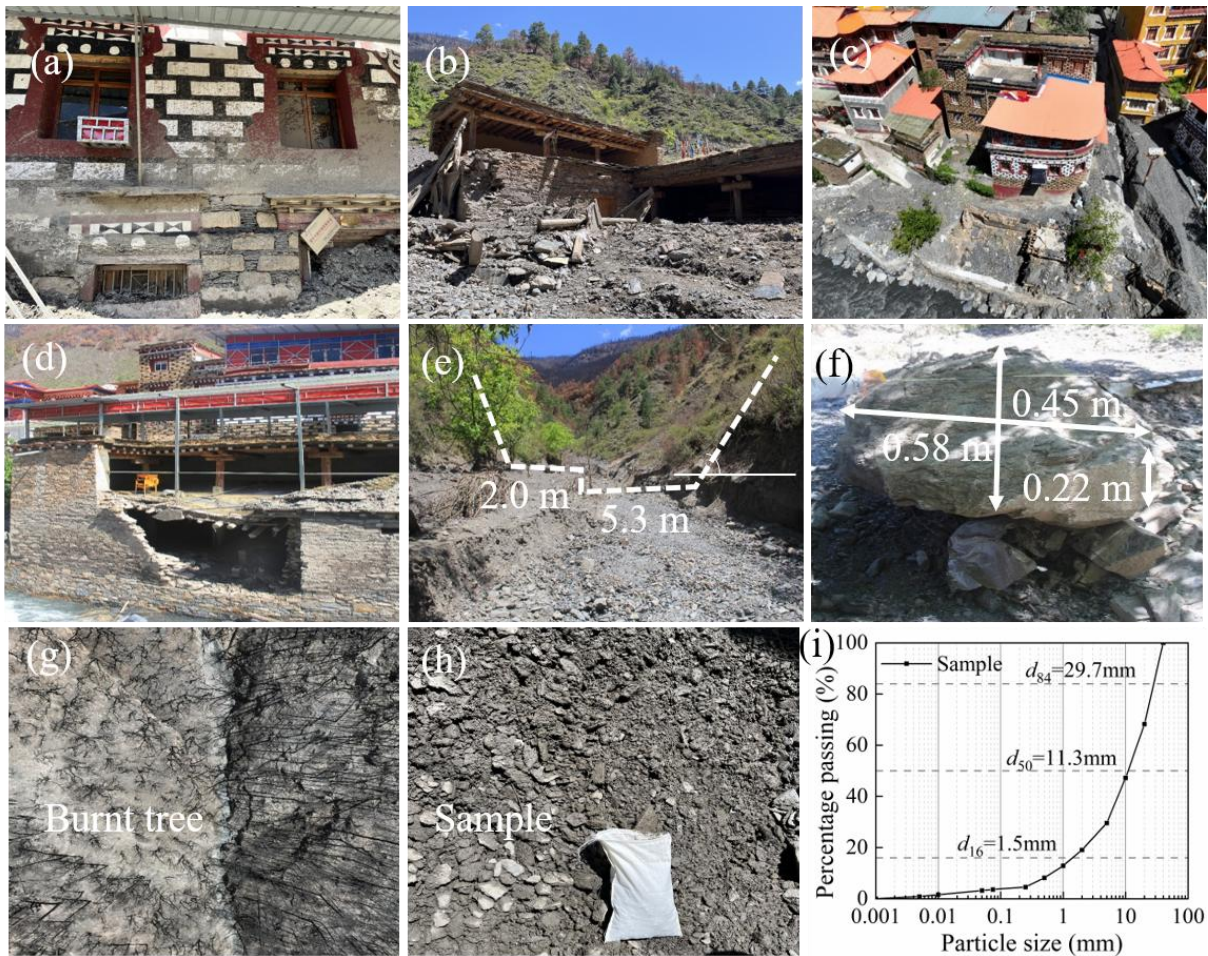


188

189 Figure 3. Hydrological characteristics: distributions of the hourly and cumulative rainfall levels.

190 **2.1.2 Field data collection**

191 An unmanned aerial vehicle (UAV) (Inspire3, DJI-Innovations; vertical accuracy: ± 0.1 m;
192 horizontal accuracy: ± 0.3 m) was employed to obtain images of the G1 and G2 gullies, which
193 were used to acquire topographic and geomorphic information of channels and the spatial
194 distribution of buildings (Fig. 5). A laser rangefinder (Contour XLRic, with a maximum range
195 of 1,850 m and a measurement accuracy of 0.10 m) was applied to measure the dimensions of
196 buildings (floor height, width, and length) and the section size of channels (width, gully bed
197 gradient, and bank slope angle) (Fig. 4). The structural type, impact azimuth, affected portion
198 and damage degree of the building were recorded with a camera (SONY A6400). The size of
199 stone blocks, thickness of the ash layer and burned soil, burial height and flow depth mark were
200 measured with a scale. The particle size of postfire debris flows was measured with vibrating
201 sieving machines (measuring range: 0.25~20 mm) and Malvern particle size analysers
202 (measuring range: 0.02-2,000 μm ; scanning speed: 1,000 Hz). Then, the samples were analysed
203 to obtain particle size distribution curve. Derived from sieving and laser analysis, the curve only
204 includes particles up to 20 mm and excludes the larger boulders documented in the field (Fig.
205 4f). Field work served as the basis for the subsequent simulations and the determination of
206 postfire debris flow physical parameters.



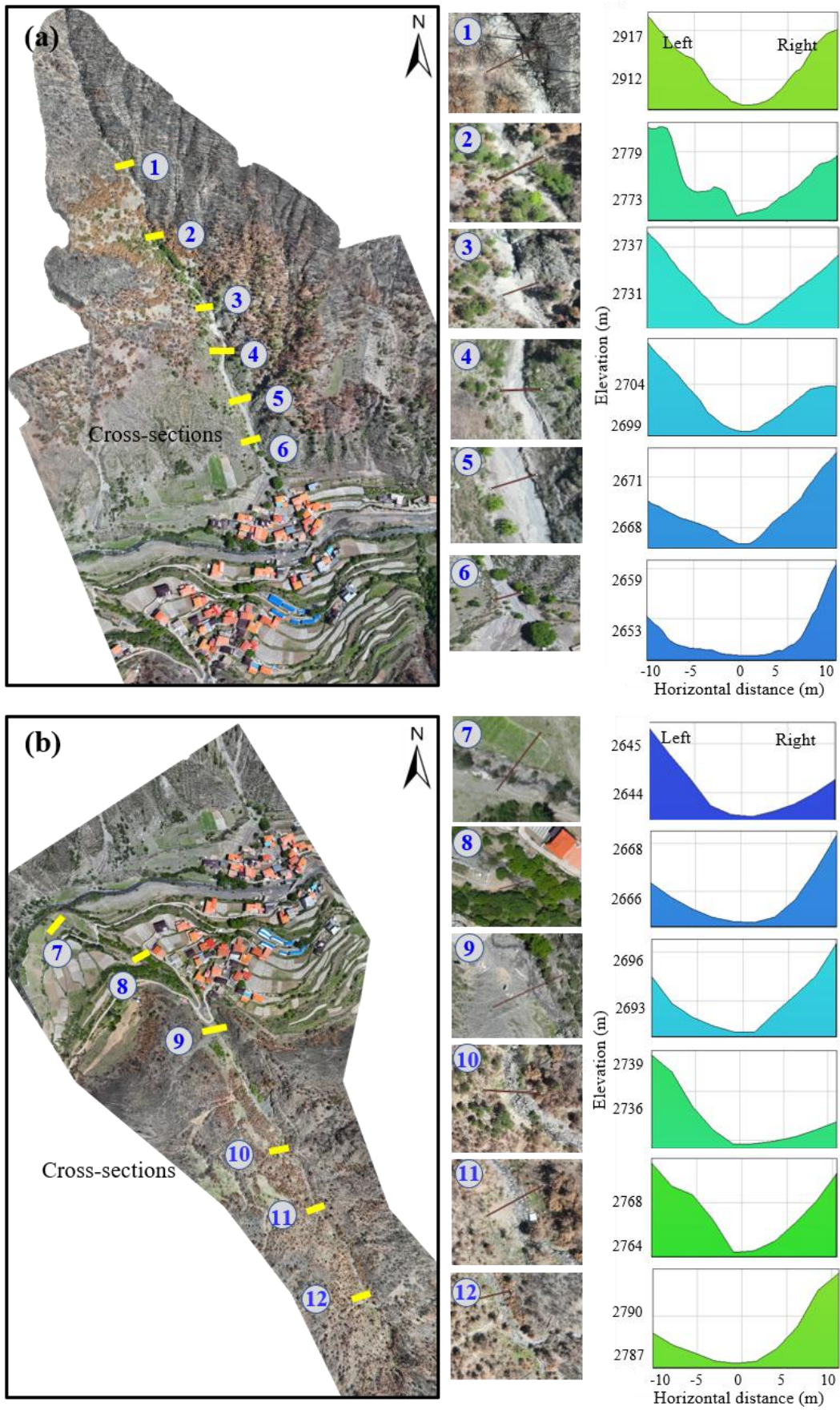
207
 208 Figure 4. Fieldwork techniques for capturing postfire debris flow events: (a)-(d) Damaged
 209 buildings; (e) channel section; (f) block stone size; (g) burned area; (h) particle sampling; (i)
 210 particle size distribution curve.

211 The obtained aerial images were subsequently processed using PhotoScan software to
 212 generate a 3D digital orthophoto in the WGS-1984 geographic coordinate system (Wang et al.
 213 2024) and to produce a digital elevation model (DEM), which served as base data for the
 214 subsequent runout analyses. These digital model data facilitated the identification of
 215 geomorphic features within the G1 and G2 catchments and the spatial distribution of damaged
 216 buildings (Fig. 5). The G1 and G2 gullies are located on the left and right banks of Kule village,
 217 respectively. G1 and G2 are spatially adjacent and exhibit similarities in terms of geological

218 setting, soil type, vegetation, catchment hydrological characteristics, fire history, and field-
 219 observed surface material composition. The catchment area of the G1 gully is small, but the
 220 longitudinal gradient of the main channel is steeper with extensive moderate-high burned areas
 221 (He et al., 2024). The catchment area of the G2 gully is large, with a gentler longitudinal
 222 gradient of the main channel and a larger relative terrain elevation difference. Twelve
 223 cross-sectional channel measurements (sections 1 to 12, six per gully) revealed that the channel
 224 width gradually increases from upstream to downstream, ranging from 2 to 10 m (Fig. 5). In
 225 Fig. 5, “horizontal distance” is lateral distance from the channel center, with zero at the center;
 226 “left” and “right” indicate the two banks of the channel. The characteristic parameters of the
 227 G1 and G2 gullies are listed in Table 1.

228 Table 1 Characteristics of the G1 and G2 gullies on both sides of Kule village, Yajiang County

| Debris flow gully | Catchment area (km ²) | Main channel length (km) | Average slope of the channel | Burned area (km ²) | Watershed relief (m) | Relative position | Debris flow event |
|----------------------|--------------------------------------|-----------------------------------|---------------------------------------|--------------------------------------|-------------------------|-------------------------------|---------------------------|
| G1 gully | 1.40 | 1.60 | 0.40 | 0.90 | 850.00 | Left bank of Kule village | Debris flows occurred |
| G2 Gully | 3.50 | 2.20 | 0.17 | 1.50 | 1015.00 | Right bank of Kule village | Debris flows may occur |



229

230 Figure 5. Characteristics of different channel cross sections: (a) G1 debris flow channel on the

231 left bank of Kule village; (b) G2 debris flow channel on the right bank of Kule village.

232 **2.1.3 Calculation of postfire debris flow parameters**

233 (1) Debris flow density

234 The particle size distribution of a given debris flow deposit can be used to determine the
235 debris flow density, which can be calculated as follows (Wang et al., 2024; Chen et al., 2021):

$$236 \quad \gamma_d = \gamma_0 + \gamma_m P_2 (P_{0.05})^{0.35} \quad (1)$$

237 where γ_d is the density of the debris flow (t/m^3); γ_m is the minimum density of a viscous
238 debris flow ($2.0 t/m^3$); γ_0 is the minimum density of the debris flow ($1.4\sim 1.5 t/m^3$); P_2 is the
239 percentage of coarse particles with a diameter greater than 2 mm; and $P_{0.05}$ is the percentage of
240 fine particles with a diameter smaller than 0.05 mm (Table 2).

241 (2) Debris flow volume

242 The US Geological Survey (USGS) debris flow hazard assessment system is based on a
243 model developed by Gartner et al. (2014) for estimating the volume of postfire debris flows.
244 The emergency assessment volume model is a multiple linear regression model and has been
245 widely applied (Rengers et al., 2023; Gorr et al., 2024). This model can be expressed as follows:

$$246 \quad \ln(V_{DF}) = 4.22 + 0.39\sqrt{I_{15}} + 0.36\ln(B_{mh}) + 0.13\sqrt{R} \quad (2)$$

247 where V_{DF} is the postfire debris flow volume (m^3); I_{15} is the 15-min maximum rainfall
248 intensity (mmh^{-1}); B_{mh} is the burned area with moderate and high burn severity levels (km^2);
249 and R is the watershed relief (m).

250 (3) Debris flow peak discharge

251 The debris flow peak discharge can be estimated via the volume-peak discharge

252 relationship method (Rickenmann 1999; Marchi et al., 2002) or the rain-flood method (Zhou et
253 al., 1991; Cui et al., 2023).

254 First, the peak discharge for a given catchment can be estimated on the basis of the debris
255 flow volume (Kang and Kim, 2016). Notably, studies have demonstrated that the debris flow
256 volume is related to the peak discharge (Navratil et al., 2013; Cui et al., 2018; Guo et al., 2024):

$$257 \quad Q_d = \alpha V_{DF}^\beta \quad (3)$$

258 where Q_d is the peak discharge of the debris flow (m^3/s); V_{DF} is the postfire debris flow
259 volume (m^3), which can be calculated by Eq. (2); and α and β are fitting coefficients for different
260 watersheds, with a specific range. Please refer to Guo et al. (2024) for further details.

261 Second, the rain-flood method can be used for calculating rainfall-triggered debris flows
262 under different rainfall frequency conditions (Zhou et al., 1991; Chang et al., 2020):

$$263 \quad Q_d = (1 + \phi) Q_f D_u \quad (4a)$$

264 where Q_f is the peak flood discharge of clean water (m^3/s); Q_d is the peak flow of the debris
265 flow (m^3/s); D_u is the blockage amplification factor; ϕ is the solids concentration, $\phi = (\gamma_d - 1) / (\gamma_s -$
266 $\gamma_d)$; and γ_d and γ_s are the densities of the debris flow and solid materials (t/m^3), respectively.

$$267 \quad Q_f = 0.278 \phi \frac{S}{\tau^n} F \quad (4b)$$

268 where ϕ is the peak runoff coefficient; S is the storm force (mm/h), namely, the maximum
269 1-h rainstorm intensity; τ is the confluence time (h); n is the rainstorm attenuation index; and F
270 is the watershed area (km^2). The parameters in Eq. (4b) can be obtained by consulting the
271 calculation manual and can be calculated as follows (Sichuan Hydrological Manual 1984; Cui
272 et al., 2023):

$$273 \quad \varphi = 1 - 1.1 \frac{\mu}{S} t_0^n \quad (5a)$$

$$274 \quad S = H_1 K_1 \quad (5b)$$

$$275 \quad t = t_0 \varphi^{-\frac{1}{4-n}} \quad (5c)$$

$$276 \quad n = 1 + 1.285 \left(\lg \frac{H_1 K_1}{H_6 K_6} \right) \quad (5d)$$

$$277 \quad \mu = 3.6 K_p F^{-0.19} \quad (5e)$$

$$278 \quad t_0 = \left(\frac{0.383}{m S^{1/4} / \theta} \right)^{\frac{4}{4-n}} \quad (5f)$$

$$279 \quad m = 0.221 \theta^{0.204} \quad (5g)$$

$$280 \quad \theta = \frac{L}{J^{1/3} F^{1/4}} \quad (5h)$$

281 where μ is the current generation parameter (mm/h); t_0 is the confluence time of the basin;
 282 H_1 and H_6 are the 1- and 6-h average rainfall amounts, respectively (mm); K_1 and K_6 are the
 283 modulus coefficients corresponding to periods H_1 and H_6 , respectively; K_p is the modulus ratio
 284 coefficient of the Pearson curve; m is the confluence parameter; θ is the watershed coefficient;
 285 J is the slope of the channel; and L is the main channel length (km).

286 Finally, we combined the results of the two peak discharge calculation methods to
 287 determine the peak discharges of the postfire debris flows in the G1 and G2 gullies at different
 288 frequencies (Fig. 6). The flow process line of debris flow discharge can be obtained by using
 289 the generalized pentagon method, which has been widely adopted in previous studies (Zhang
 290 et al., 2023; Ding et al., 2023).



291

292 Figure 6. Flow hydrographs of the G1 and G2 gullies at different frequencies.

293 Table 2. Key input parameters coefficient for debris flow calculations.

| Parameters | P_2 | $P_{0.05}$ | I_{15} | B_{mh} | α | β | D_u | φ | S | τ | n | μ | θ |
|------------|-------|------------|----------|----------|----------|---------|-------|-----------|-------|--------|------|-------|----------|
| Value | 0.81 | 0.03 | 7.00 | 0.90 | 0.46 | 0.44 | 1.50 | 0.89 | 18.20 | 0.21 | 0.21 | 3.37 | 1.99 |

294 2.2 FLO-2D numerical simulation of disaster scenarios

295 2.2.1 Governing equations for rainfall runoff and debris flows

296 The two-dimensional numerical debris flow evolution model FLO-2D was applied to
 297 simulate the runout process and to quantify key metrics of debris flows in the G1 and G2 gullies
 298 (Wang et al., 2024; Si et al., 2022; Zhang et al., 2018; Chang et al., 2020). On the basis of 2D
 299 shallow water equations, mass and momentum conservation equations are employed in the
 300 FLO-2D model as the governing equations:

$$301 \quad i = \frac{\partial h}{\partial t} + \frac{\partial h \partial V_x}{\partial x} + \frac{\partial h \partial V_y}{\partial y} \quad (6a)$$

$$302 \quad S_{f_x} = S_{ox} - \frac{\partial h}{\partial x} - \frac{V_x}{g} \frac{\partial V_x}{\partial x} - \frac{V_y}{g} \frac{\partial V_x}{\partial y} - \frac{1}{g} \frac{\partial V_x}{\partial t} \quad (6b)$$

$$303 \quad S_{f_y} = S_{oy} - \frac{\partial h}{\partial y} - \frac{V_y}{g} \frac{\partial V_y}{\partial y} - \frac{V_x}{g} \frac{\partial V_y}{\partial x} - \frac{1}{g} \frac{\partial V_y}{\partial t} \quad (6c)$$

304 where h is the flow depth; V_x and V_y are the depth-averaged velocities along the horizontal
 305 x and y coordinates, respectively; i is the intensity at the flow surface; and S_{f_x} and S_{f_y} are the
 306 friction slopes, expressed as functions of bed slopes S_{ox} and S_{oy} , respectively, the pressure
 307 gradient and the convective and local acceleration terms (Chen et al., 2021). The total friction
 308 slope, S_f , is the sum of the yield slope, the viscous slope, and the turbulent dispersive slope
 309 (Zhang et al., 2018), which can be obtained as follows:

$$310 \quad S_f = \frac{\tau_y}{\gamma_m h} + \frac{K\eta v}{8\gamma_m h^2} + \frac{n^2 v^2}{h^{4/3}} \quad (7)$$

311 where n is Manning's coefficient; K is flow resistance parameter; η is the dynamic viscosity
 312 (Pa·s), and τ_y is the yield stress (Pa), which can be calculated as follows:

$$313 \quad \eta = \alpha_1 e^{\beta_1 C_v} \quad (8a)$$

$$314 \quad \tau_y = \alpha_2 e^{\beta_2 C_v} \quad (8b)$$

315 where C_v is the sediment concentration, and α_1 , α_2 , β_1 , and β_2 are empirical coefficients.

316 The FLO-2D simulations were conducted by adding elevation data of the computation area
 317 to the grid, which was set to 5 m×5 m, after which the inlet and outlet conditions, the rheological
 318 parameters (Table 3), the duration of the debris inflow hydrograph (i.e., 30 min) and the peak
 319 discharge were defined. Manning's roughness coefficient of 0.1 is selected referring to the
 320 FLO-2D manual, and the same value adopted in previous studies (Zhang et al., 2018; Chen et
 321 al., 2021). Finally, the dynamics and key parameters, such as the flow depth and flow velocity,

322 were obtained.

323 Table 3. the rheological parameters for the debris flow simulation.

| Parameters | | Value |
|---|------------|---------|
| Manning's roughness coefficient (n) | | 0.10 |
| Flow resistance parameter (K) | | 2,280 |
| Sediment concentration (C_v) | | 0.49 |
| Viscosity coefficients | α_1 | 0.81 |
| | β_1 | 13.72 |
| Yield stress coefficients | α_2 | 0.00462 |
| | β_2 | 11.24 |

324 2.2.2 Model calibration and validation

325 To ensure accuracy, the methodology proposed by Scheidl and Rickenmann (2010) was
326 adopted to validate the simulation results (Table 4). We measured the observed depositional fan
327 area through field investigations and the predicted depositional fan area obtained with the FLO-
328 2D model (Chen et al., 2021). The subareas (X, Y and Z) were obtained via the overlay of the
329 predicted deposition area with the observed deposition area. We assessed the overall
330 reconstruction accuracy via the following evaluation parameters (Chen et al., 2021; Wang et al.,
331 2024):

$$332 \quad \varepsilon = \frac{S_X}{S_{observed}} - \frac{S_Y}{S_{observed}} - \frac{S_Z}{S_{observed}} + \frac{V_X}{V_{observed}} \quad (9)$$

$$333 \quad \delta = \frac{\varepsilon + 2}{4} \quad (10)$$

334 where S_X , S_Y , and S_Z are the positive accuracy region, negative accuracy region, and
335 missing accuracy region, respectively; $S_{observed}$ is the actual impact zone; V_X is the correct
336 judgement volume; $V_{observed}$ is the actual volume; and δ is the normalized accuracy value, with

337 values ranging from 0 to 1.

338 Table 4 Calibration parameters and accuracy of the numerical simulation results

| Parameters | S_x | S_y | S_z | S_{observed} | V_x | V_{observed} | ε | δ |
|-------------|------------------------|------------------------|------------------------|------------------------|------------------------|------------------------|---------------|----------|
| | (10^3 m^2) | (10^3 m^2) | (10^3 m^2) | (10^3 m^2) | (10^4 m^3) | (10^4 m^3) | | |
| Impact zone | 13.59 | 1.83 | 1.06 | 15.42 | 0.73 | 0.81 | 1.59 | 0.90 |

339 2.3 Development of empirical vulnerability models for buildings

340 2.3.1 Damage class of buildings

341 Kule village encompasses a total of 128 buildings, with 36 buildings on the left bank
342 affected by postfire debris flows in the G1 gully. The damage to buildings notably depends on
343 their structural type, material resistance and distribution density (Zhang et al., 2018). In the
344 study area, 95% of the affected main building structures are BC structural-type buildings, which
345 are widely distributed in mountainous areas across China (Chen et al., 2021). We subsequently
346 aimed to develop vulnerability curves for BC buildings. Most buildings in the study area
347 comprise 1-3 floors, and the building height ranges from 3-8 m. To determine the degree of
348 damage to buildings caused by debris flows, it is necessary to establish a classification standard
349 on the basis of the actual structural and damage degree conditions (Hu et al., 2012; Lee et al.,
350 2024). Table 5 provides the four categories of damage to a given structure and the corresponding
351 vulnerability index values, including slight, moderate, extensive, and complete damage. On the
352 basis of the above assumptions and analysis, damaged buildings affected by debris flows in
353 Kule village were constructed (Appendix A).

354 Table 5 Damage classes and definitions for buildings (Hu et al., 2012; Wang et al., 2024; Lee
355 et al., 2024)

| Damage class | Damage description | Value |
|--------------|--|---------|
| Slight | Minor nonstructural damage occurred, with no impact on stability; damage was limited to furnishings and fittings. | 0.1~0.3 |
| Moderate | Cracks appeared in the wall, but stability remained unaffected; repairs are not urgent. | 0.3~0.6 |
| Extensive | The structure is partly destroyed, with partial loss of external and internal walls; evacuation is necessary; and reconstruction of damaged parts is required. | 0.6~0.8 |
| Complete | The structure is completely destroyed; evacuation is imperative; and complete reconstruction is necessary. | 0.8~1.0 |

356 2.3.2 Debris flow intensity

357 In this study, six commonly used debris flow intensities were selected as multidimensional
358 indicators of the destruction potential (Quan Luna et al., 2011; Eidsvig et al., 2014; Kang and
359 Kim, 2016; Zhang et al., 2018; Chen et al., 2021; Wang et al., 2024; Lee et al., 2024), including
360 the flow depth (h), flow velocity (v), impact pressure (p), momentum flux (f), overturning
361 moment (m), and relative burial height (b).

362 The flow impact pressure includes both hydrostatic and hydrodynamic forces (Kang and
363 Kim, 2016; Wang et al., 2024), and the total impact pressure exerted by a debris flow can be
364 expressed as:

$$365 \quad p = \frac{1}{2} \rho g h + \rho v^2 \quad (11)$$

366 where p is the impact pressure (Pa); v is the flow velocity (m/s); and h is the flow depth
367 (m), ρ is the debris flow density (kg/m³).

368 The momentum flux can be obtained by multiplying the flow depth and the square of the

369 flow velocity (Jakob et al., 2012; Chen et al., 2021):

$$370 \quad f = hv^2 \quad (12)$$

371 where f is the momentum flux (m^3/s^2).

372 The overturning moment of a debris flow is related to the maximum flow velocity and
373 depth at which it collides with a given structure, as reported by Zhang et al. (2018):

$$374 \quad m = vh \quad (13)$$

375 where m is the overturning moment (m^2/s).

376 The relative burial height is defined by the deposition height and the affected building
377 height to represent the degree of burial damage (Totschnig et al., 2011; Zhang et al., 2018):

$$378 \quad b = \frac{h_d}{h_b} \quad (14)$$

379 where b is the relative burial height, h_d is the deposition height (m), and h_b is the building
380 height (m).

381 Under the same damage state, vulnerability values derived from different intensity
382 indicators may vary, potentially leading to inconsistent damage classification (Luo et al., 2023).

383 To enable a direct comparison of indicator performance in Discussion Section 4.1 (note that
384 normalized values are used exclusively for the analysis in that section), both intensity and
385 vulnerability values were normalized using the following equations (Zhang et al., 2024):

$$386 \quad I^* = \frac{I - \min(I)}{\max(I) - \min(I)} \quad (15a)$$

$$387 \quad V^* = \frac{V - \min(V)}{\max(V) - \min(V)} \quad (15b)$$

388 where I^* and V^* are the normalized values of the debris flow intensity and vulnerability,

389 respectively.

390 2.3.3 Vulnerability curve

391 The vulnerability model captures the relationship between the probability of building
392 damage reaching a certain state and the debris flow intensity (Cui et al., 2011). Notably,
393 postdisaster data-driven vulnerability curves can be expressed via function models (Fuchs et al.,
394 2019). Currently, many vulnerability functions, such as logistic, Weibull, exponential, power-
395 law and Avrami functions, are employed (Quan Luna et al., 2011; Eidsvig et al., 2014; Chen et
396 al., 2021; Lee et al., 2024). However, the uncertainties in these models originate from the curve
397 fitting process. For example, the use of the exponential function cannot guarantee that the curve
398 passes through the origin. Therefore, recent studies have indicated that lognormal cumulative
399 distribution function (LNCDF) vulnerability curves provide better performance (Luo et al.,
400 2023):

$$401 \quad V = \Phi \left[\frac{1}{\beta} \ln \left(\frac{I}{I_m} \right) \right] \quad (16)$$

402 where β is the standard deviation of the logarithm of the hazard intensity; I is the debris
403 flow hazard intensity; I_m is the median hazard intensity; V is vulnerability value (0-1); and Φ is
404 the LNCDF, which can be expressed as follows:

$$405 \quad \Phi(x) = \int_0^x \frac{1}{\sqrt{2\pi}\sigma t} e^{-\frac{(\ln(t)-\mu)^2}{2\sigma^2}} dt \quad (17)$$

406 where μ is the mean of the LNCDF, and σ is the standard deviation of the LNCDF.

407 The performance of models was comparatively analysed via four dimensionless
408 performance indices, namely, the coefficient of determination (R^2), the mean relative error

409 (MRE), the Theil inequality coefficient (TIC), and the prediction accuracy factor (PAF).
 410 Notably, lower MRE and TIC values reflect higher model performance. Additionally, the closer
 411 the PAF value is to 1, the better the agreement between the calculated and experimental values
 412 (the higher the prediction accuracy). These indices can be calculated as follows (Lee et al., 2024;
 413 Wang et al., 2018):

$$414 \quad R^2 = 1 - \frac{\sum_{i=1}^N (I_{cal,i} - I_{obs,i})^2}{\sum_{i=1}^N (I_{cal,i} - \bar{I}_{obs,i})^2} \quad (18)$$

$$415 \quad MRE = \frac{1}{N} \sum_{i=1}^N \frac{|I_{cal,i} - I_{obs,i}|}{I_{obs,i}} \quad (19)$$

$$416 \quad TIC = \frac{\sqrt{\left(\sum_{i=1}^N (I_{cal,i} - I_{obs,i})^2\right) / N}}{\sqrt{\left(\sum_{i=1}^N I_{cal,i}^2\right) / N} + \sqrt{\left(\sum_{i=1}^N I_{obs,i}^2\right) / N}} \quad (20)$$

$$417 \quad PAF = 10^{\frac{\sum_{i=1}^N \log|I_{cal,i} / I_{obs,i}|}{N}} \quad (21)$$

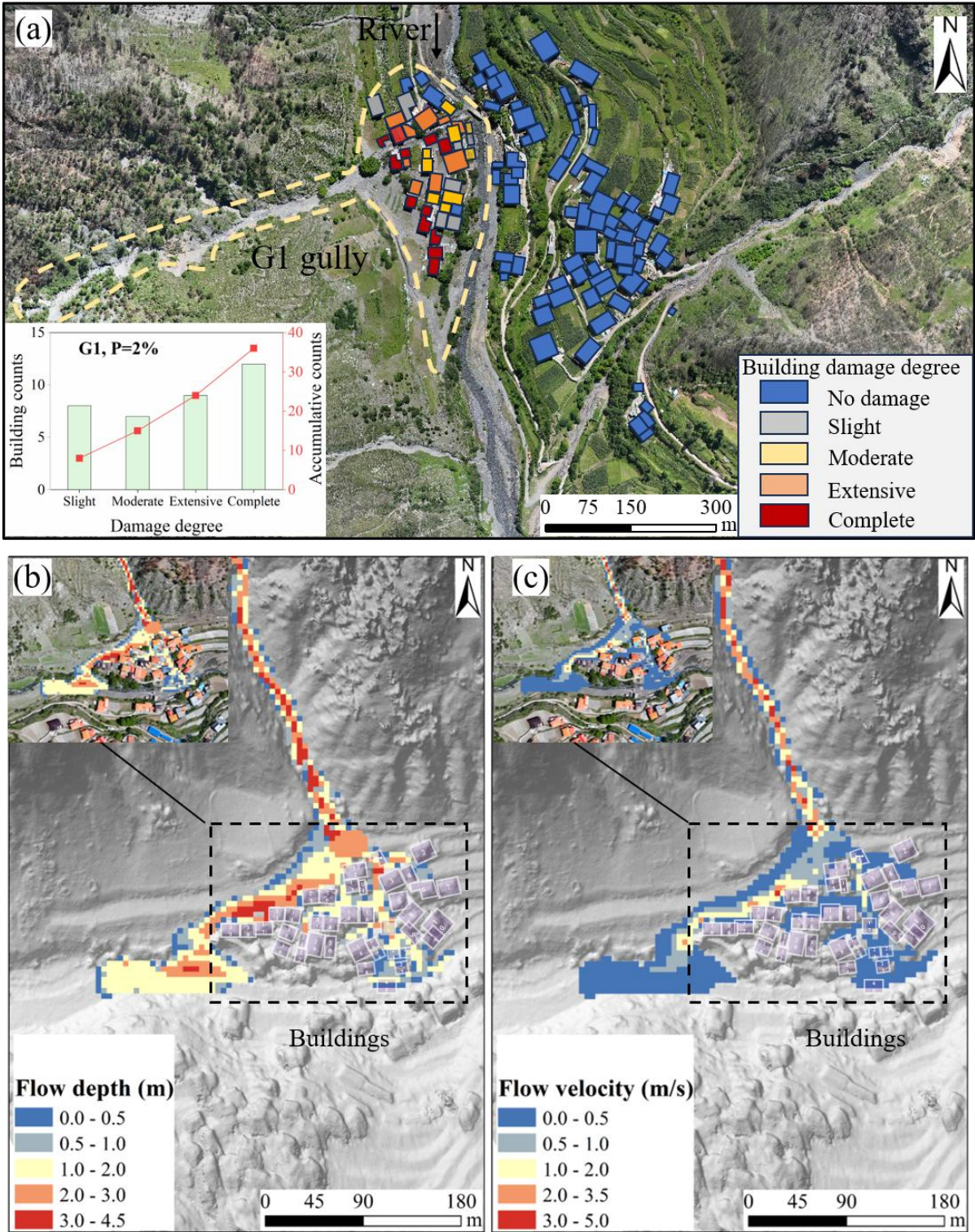
418 where N is the total number of data points, and $I_{cal,i}$ and $I_{obs,i}$ are the calculated and observed
 419 values of case i , respectively.

420 **3. Results**

421 **3.1 Reproduction of the debris flow intensity and building damage in the G1 gully**

422 Fig. 7a shows the characteristics of the degree of damage to buildings and the distribution
 423 of buildings in the G1 gully. There are 36 buildings on the left bank of Kule village affected by
 424 postfire debris flows in the G1 gully. Notably, the numbers of buildings with slight, moderate,
 425 extensive and complete damage are 8, 7, 9 and 12, respectively. Fig. 7b shows that the FLO-2D
 426 simulations reproduce the runout process of debris flows in the G1 gully that occurred on 10

427 May 2024, and distribution maps of the inundation area, flow velocity and flow depth were
428 obtained. The buildings were impacted and buried by debris flows, the flow depth near the
429 impacted buildings ranged from 0.25 to 2.61 m, and the flow velocity near the buildings ranged
430 from 0.04 to 1.93 m/s. This occurred because the debris flow energy partly dissipates under the
431 influence of building groups, and sediment is deposited inside the buildings. The debris flow
432 also partially entered the main river, causing blockages at bridges connecting the villages on
433 both sides (Fig. 7c).



434

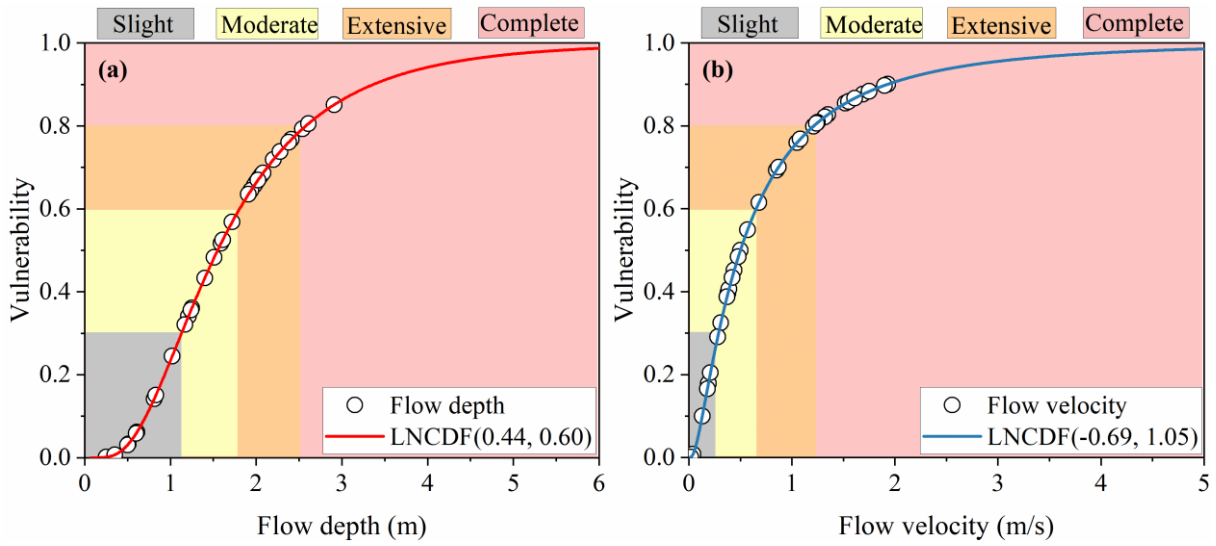
435 Figure 7. Building damage from field survey and debris flow reconstruction using FLO-2D in

436 the G1 gully: (a) Distribution and statistics of building damage; (b) flow depth map; (c) flow

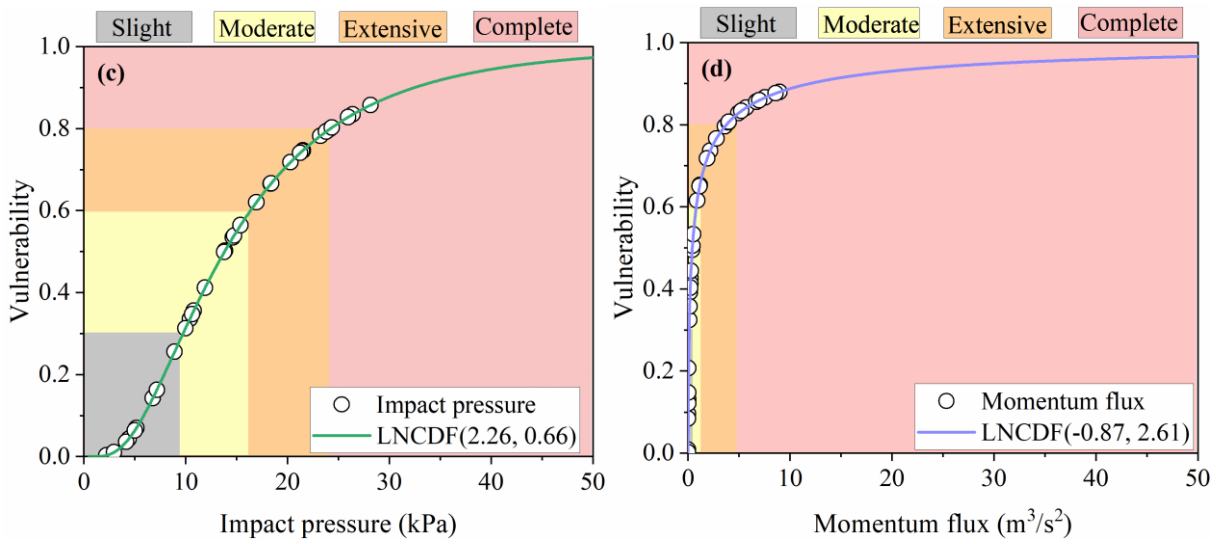
437 velocity map.

438 3.2 Development of the vulnerability model

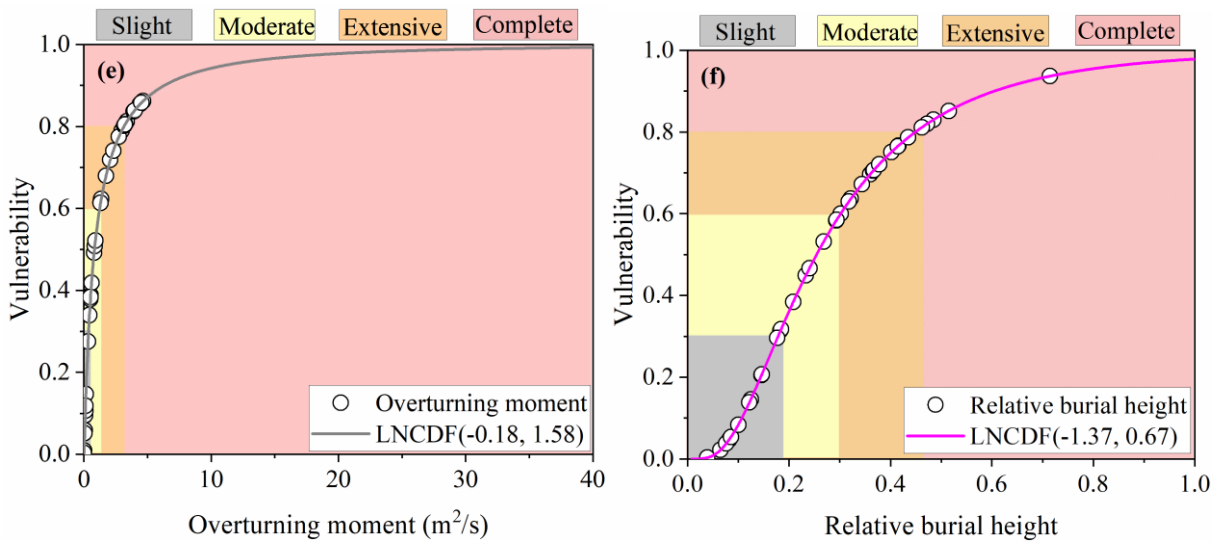
439 Fig. 8 shows six groups of developed vulnerability curves for the 2024 postfire debris flow
440 events in the G1 gully, including the flow depth, flow velocity, impact pressure, momentum
441 flux, overturning moment and relative burial height. The vulnerability curve can be obtained
442 via a continuum function relating the debris flow intensity (X-axis) to the degree of building
443 damage (Y-axis). The LNCDF effectively described the trend in the data. Each vulnerability
444 curve is a monotonically increasing function, indicating that with increasing debris flow
445 intensity, the probability of failure gradually increases. When the slope of the vulnerability
446 curve suddenly increases, the ability of the structure to resist disasters rapidly decreases after
447 critical-strength debris flow disaster occurrence, leading to a rapid increase in the probability
448 of failure. Specifically, to reach a maximum vulnerability value of 1, BC buildings necessitate
449 a flow depth greater than 6 m, a flow velocity of 5 m/s, an impact pressure of 50 kPa, a
450 momentum flux of $50 \text{ m}^3/\text{s}^2$, and an overturning moment of $40 \text{ m}^2/\text{s}$. However, completely
451 damaged buildings (with a vulnerability value exceeding 0.8) can no longer function properly.
452 Thus, the critical value of failure is lower, corresponding to a flow depth of 2.5 m, a flow
453 velocity of 1.3 m/s, an impact pressure of 25 kPa and a relative burial height of 0.48.
454 Additionally, the responses of the various indicators to vulnerability differed, and these
455 differences are analysed in greater detail in the subsequent chapter.



456



457



458

459 Figure 8. Vulnerability curves for debris flow intensities: (a) Flow depth, (b) flow velocity, (c)

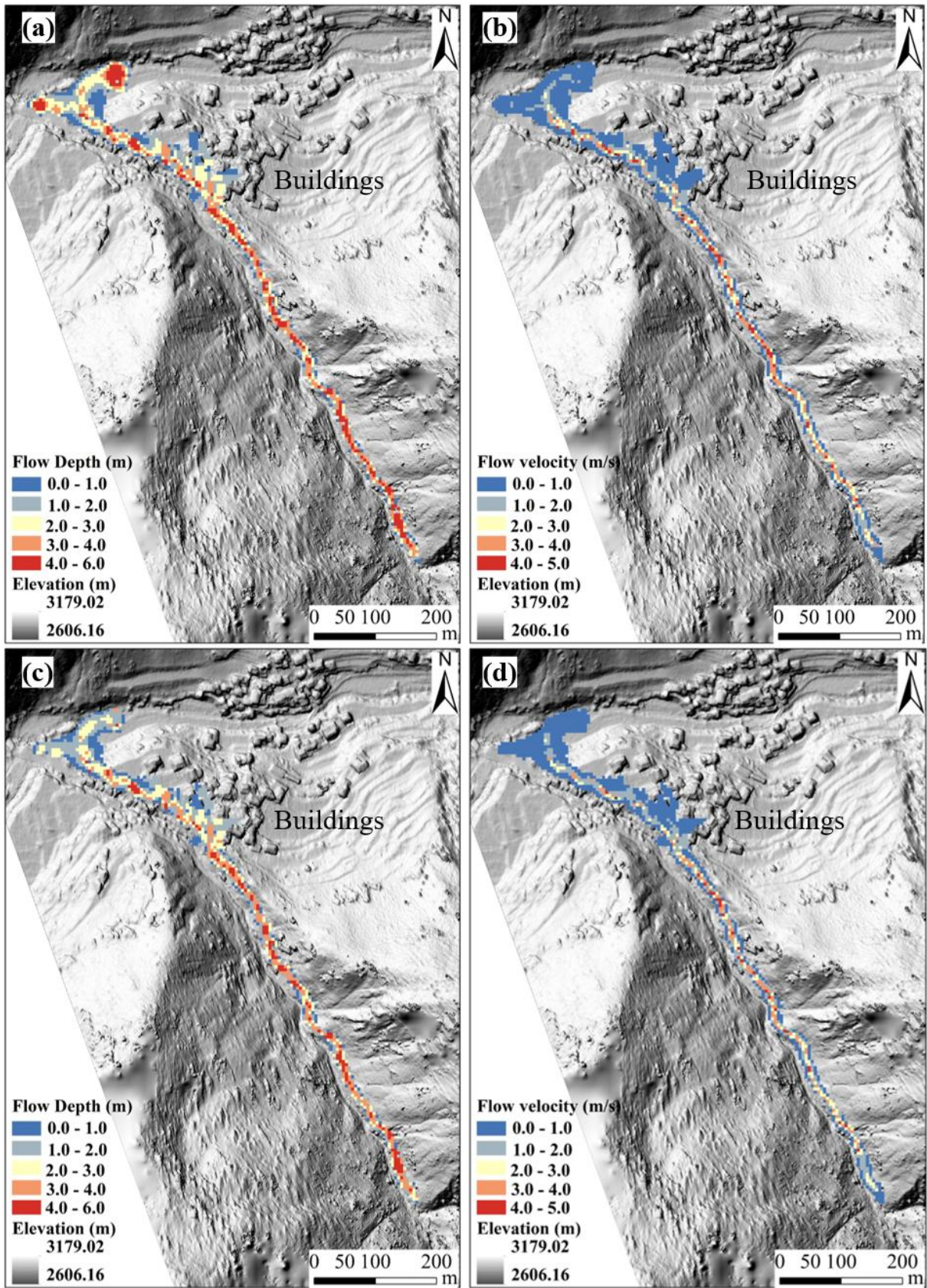
460 impact pressure, (d) momentum flux, (e) overturning moment, and (f) relative burial height.

461 The legend “LNCDF (μ, σ)” denotes the lognormal cumulative distribution function (LNCDF),
462 where μ is the mean and σ is the standard deviation for each curve.

463 **3.3 Application of the vulnerability model in the G2 gully**

464 Potential postfire debris flow events may occur in the G2 gully, thus posing a serious threat
465 to buildings on the right bank of Kule village. Fig. 9 shows the prediction of potential debris
466 flows in the G2 gully using the FLO-2D model under reproduction frequency conditions of P=2%
467 (the peak flow is 40 m³/s) and P=1% (the peak flow is 48 m³/s). The simulated scenarios
468 revealed that the buildings near the channel were significantly affected by the debris flow, and
469 the debris flow flowed into the main river, causing deposition and blockage. The maximum
470 flow depth and flow velocity around the buildings are 3.50 m and 2.36 m/s, respectively. A
471 comparison of the flow depths between the two recurrence periods revealed that the maximum
472 value under P=1% surpassed that under P=2 by 20%.

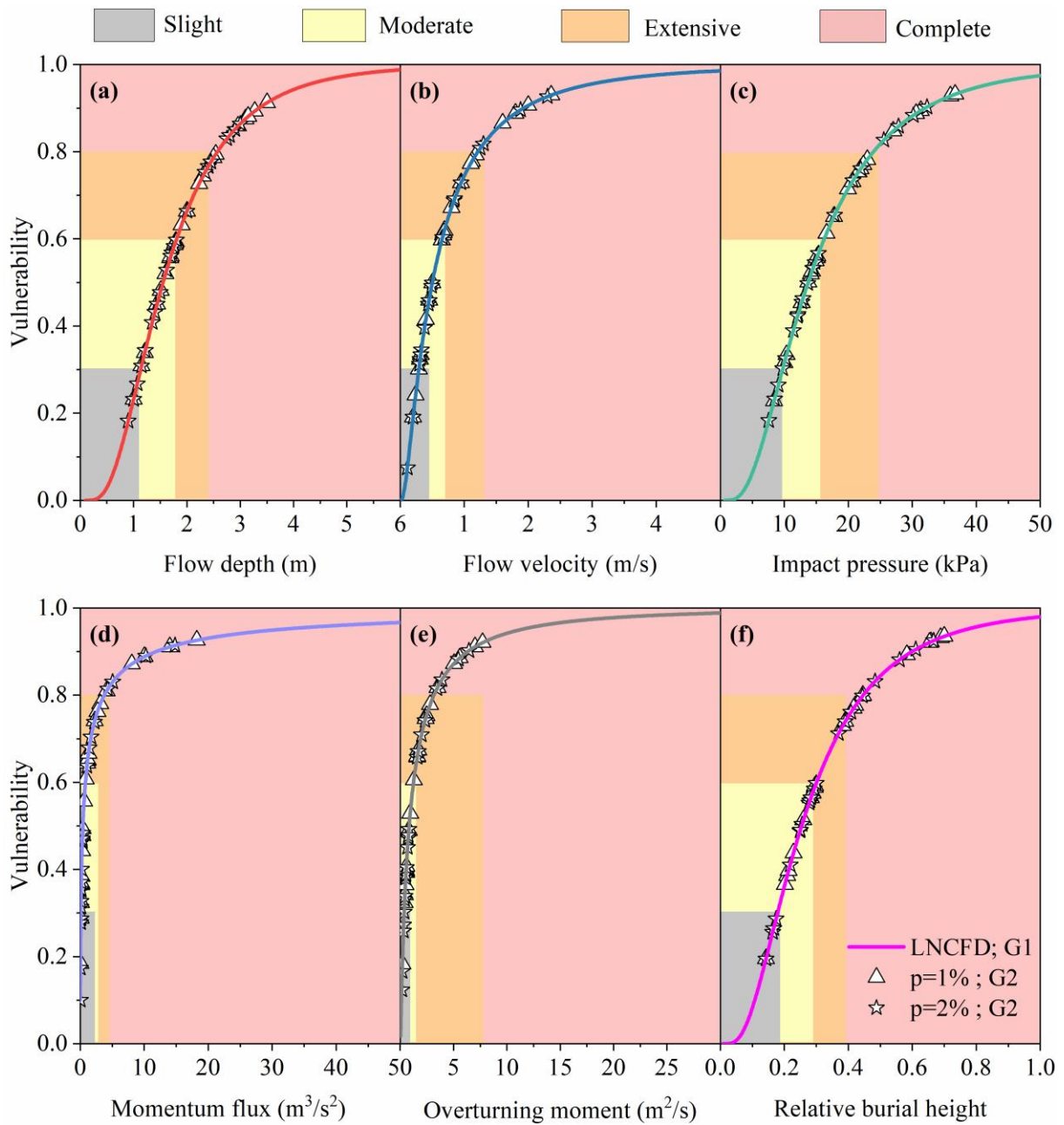
473 Then, by applying the established vulnerability model to the debris flow intensity data of
474 the G2 gully (Fig. 10), the vulnerability value of damaged buildings in the G2 gully can be
475 calculated from the generated curves (Appendix B). Next, four categories were determined
476 through a combination of vulnerability values and the damage classification system. Fig. 11
477 shows the predicted building damage degree and the spatial distribution under different
478 recurrence periods. The predicted total number of affected buildings is 24, and the numbers of
479 buildings with slight, moderate, extensive and complete damage are 4, 12, 4 and 4, respectively,
480 for P=2%. Concurrently, the numbers of buildings with extensive and complete damage exhibit
481 a corresponding uptick under longer recurrence periods (Fig. 12).



482

483 Figure 9. Prediction of the potential debris flow in the G2 gully using the FLO-2D model: (a)

484 Flow depth, P=2%; (b) flow velocity, P=2%; (c) flow depth, P=1%; (d) flow velocity, P=2%.



485

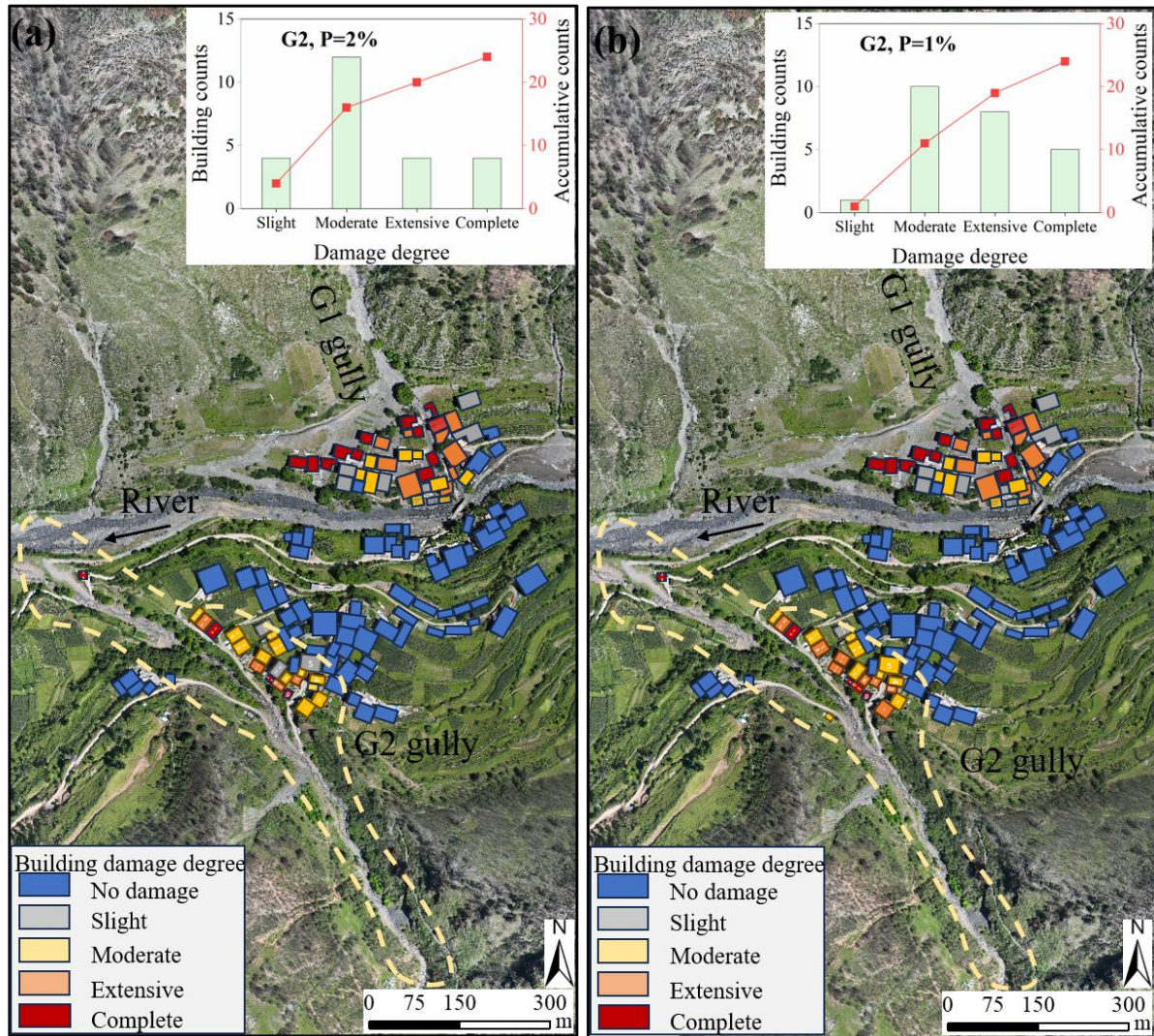
486

487

488

489

Figure 10. Vulnerability curves for different intensities of debris flows in the G2 gully according to the established vulnerability model for determining the building damage status: (a) Flow depth, (b) flow velocity, (c) impact pressure, (d) momentum flux, (e) overturning moment, and (f) relative burial height.



490

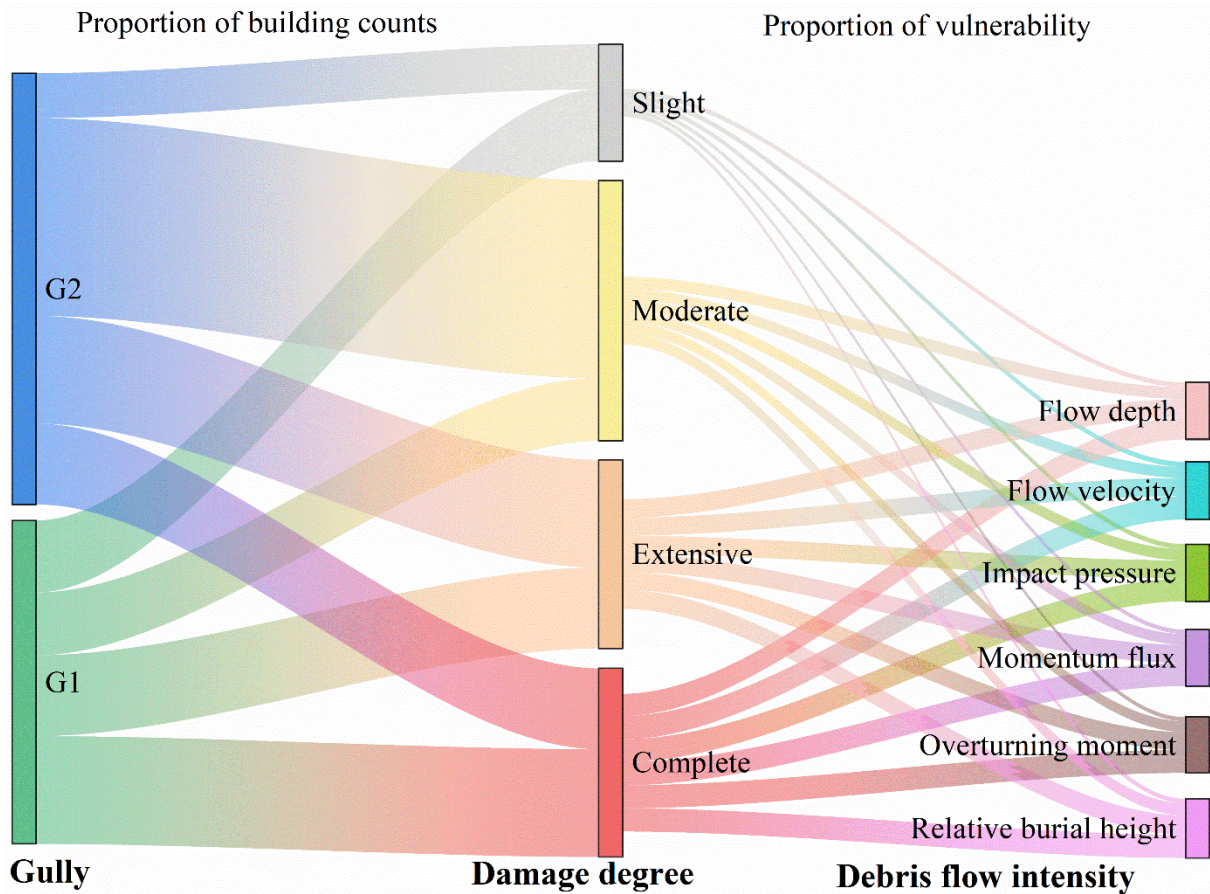
491 Figure 11. Predicted building counts with degree of damage and the spatial distribution in the
 492 G2 gully under different recurrence periods: (a) P=2%; (b) P=1%.

493 4. Discussion

494 4.1 Comparison of building vulnerability models

495 Firstly, we compared different debris flow intensity indicators. As mentioned earlier, we
 496 selected six indicators of the debris flow intensity to construct a building vulnerability model,
 497 but the vulnerability values also varied among the different indicators. Fig. 12 shows the
 498 statistics of the total number of buildings and the vulnerability value under six debris flow

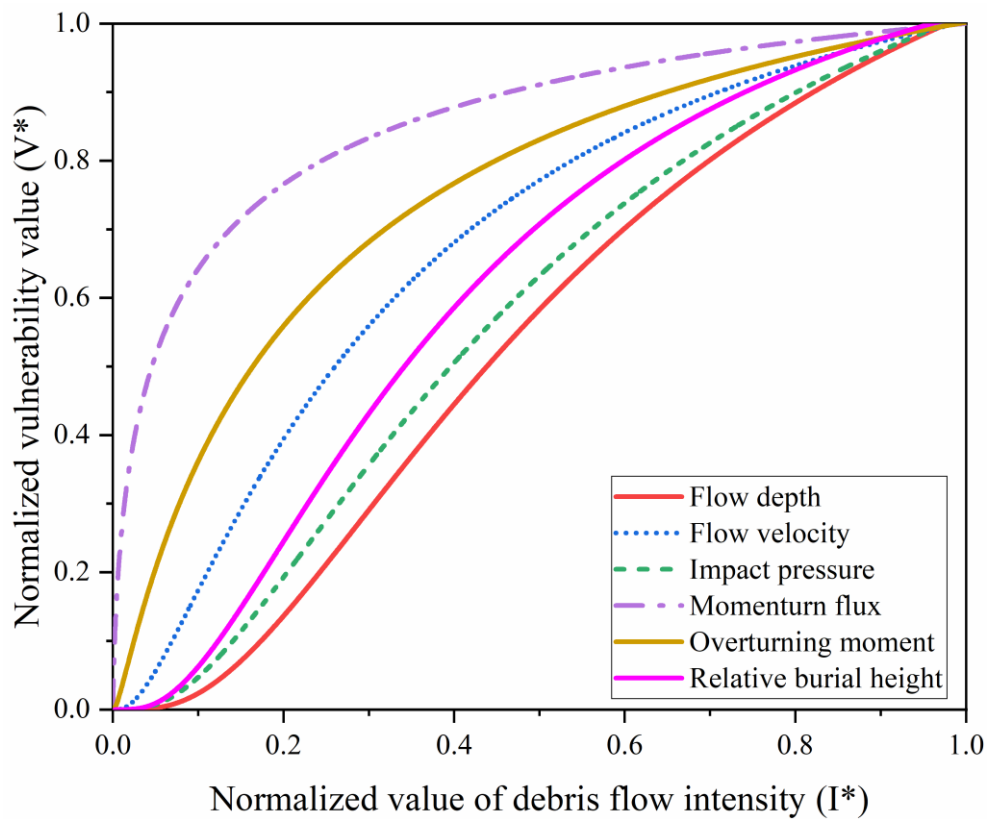
499 intensities and four damage degrees in the G1 and G2 gullies of Kule village. The line width
 500 indicates the number of damaged buildings and their vulnerability value, with a thicker line
 501 indicating a higher value. The buildings in Kule village mainly exhibited moderate and
 502 complete damage.



503
 504 Figure 12. Statistics on the number of buildings and vulnerability under different debris flow
 505 intensities and damage degrees in the G1 and G2 gullies of Kule village.

506 The differences and sensitivities of the six curves in evaluating the vulnerability of
 507 damaged buildings are compared (Fig. 13). In terms of the properties of the normalized LNCDF
 508 curves, the larger the mean (μ) value is, the more the curve shifts to the right, indicating an
 509 increased probability of I^* attaining a larger value. The higher the standard deviation (σ) is, the
 510 flatter the curve and the more dispersed the probability distribution. Conversely, the lower σ ,

511 the steeper the curve is, indicating a narrower range of I^* values and a more concentrated
512 probability distribution. As shown in Fig. 13, the momentum flux and overturning moment
513 curves are steeper, indicating higher sensitivity of these indicators accompanied by a rapid
514 increase in the probability of failure and more effective determination of the boundaries of the
515 different damage categories (Barnhart et al., 2024). Additionally, the flow depth and impact
516 pressure curves are relatively gradual, with low sensitivity, but the stability and accuracy of
517 determining the degree of damage are greater (Wang et al., 2024; Lee et al., 2024). Furthermore,
518 the impact pressure provides a more intuitive physical interpretation, indicating the
519 destructiveness of debris flows in relation to both the hydrostatic pressure and dynamic
520 overpressure, which has facilitated its widespread adoption in disaster risk assessment (Quan
521 Luna et al. 2011; Wang et al., 2024).



522
523 Figure 13. Comparison of vulnerability curves of the normalized debris flow intensity.

524 Secondly, we compared the proposed vulnerability model. Table 6 shows a comparison
525 between the proposed vulnerability models for BC buildings and models established in previous
526 studies (Quan Luna et al. 2011; Eidsvig et al. 2014; Kang and Kim, 2016; Zhang et al., 2018;
527 Chen et al., 2021; Wang et al., 2024; Lee et al., 2024). Fig. 14 shows a comparison of the
528 proposed vulnerability curves for different debris flow intensities. For flow depth (Fig. 14a),
529 our curve aligns closely with Quan Luna et al. (2011) and Zhang et al. (2018), while falling
530 between the curves of Wang et al. (2024) and Kang and Kim (2016). The complete damage
531 threshold ($V=0.8$) occurs at 2.5 m in this study, compared to 1.3 m in Wang et al. (2024). For
532 flow velocity (Fig. 14b), our curve exhibits a steeper slope than those of Zhang et al. (2018)
533 and Kang and Kim (2016). The impact pressure curve (Fig. 14c) shows an initially steep slope
534 similar to Zhang et al. (2018), then flattens as it approaches complete damage, reaching 25 kPa
535 at $V=0.8$. This value is lower than the 30 kPa reported by Quan Luna et al. (2011), Kang and
536 Kim (2016), and Lee et al. (2024). For momentum flux (Fig. 14d), our curve resembles that of
537 Chen et al. (2021) but lies well below Zhang et al. (2018). Complete damage ($V=1.0$) occurs at
538 $90 \text{ m}^3/\text{s}^2$ in this study, compared to $131 \text{ m}^3/\text{s}^2$ in Zhang et al. (2018). The overturning moment
539 curve (Fig. 14e) is steeper than that of Zhang et al. (2018), reaching $V=0.8$ at $4.0 \text{ m}^2/\text{s}$ compared
540 to $20.1 \text{ m}^2/\text{s}$. For relative burial height (Fig. 14f), our curve is considerably steeper than Zhang
541 et al. (2018).

542 The observed differences between our vulnerability curves and those established in
543 previous studies may be attributed to a combination of factors. At a general level, variations in
544 regional building codes, construction practices, building geometry, and debris flow

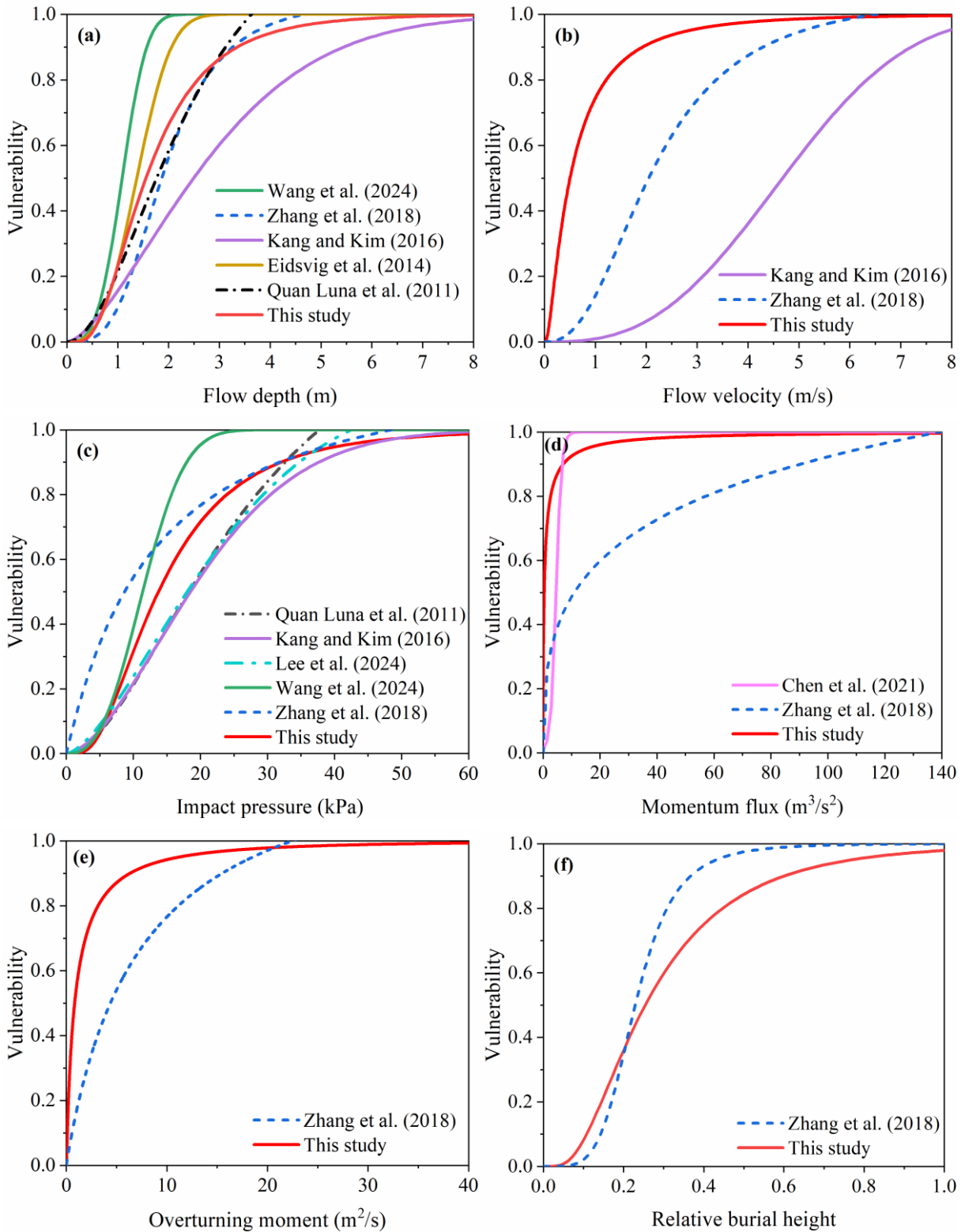
545 characteristics (e.g., volume, density, event scale) across study areas can influence vulnerability
546 thresholds (Kang and Kim, 2016; Zhang et al., 2018). However, the distinct nature of postfire
547 debris flows in this study likely plays a more important role. Wildfires alter watershed
548 conditions in ways that increase the complexity and variability of debris flow processes. First,
549 fire increases the proportion of loose, fine particles in surface soil (Ouyang et al., 2023), which
550 are easily entrained and lead to higher solid concentrations and a greater tendency for deposition
551 and building inundation. This may explain the higher complete damage thresholds observed for
552 flow depth and relative burial height. Second, fire-damaged root systems and reduced slope
553 infiltration capacity result in more pronounced sheet erosion and numerous small runoffs after
554 rainfall, subjecting buildings to multi-directional and uneven impacts. Burned basins also
555 exhibit lowered rainfall thresholds for debris flow initiation, leading to higher event frequency
556 over extended periods (Fraser et al., 2022; Ouyang et al., 2023). These factors likely contribute
557 to the steeper slopes of our flow velocity and overturning moment curves. Third, high
558 temperatures from fire can weaken building envelopes, lowering their initial resistance to
559 dynamic impact. This may explain the lower impact pressure (25 kPa) required to reach $V=0.8$
560 and the lower momentum flux threshold ($90 \text{ m}^3/\text{s}^2$) for complete damage compared to non-
561 postfire settings. Collectively, these postfire-specific mechanisms introduce greater variability
562 into intensity-damage relationships and explain the deviations between our curves and those
563 derived from non-postfire settings.

564

565

566 Table 6 Comparison of the vulnerability curves of brick-concrete buildings for different debris
 567 flow intensities between this study and previous studies

| Researchers | Debris flow density | Vulnerability functions | Vulnerability model for BC buildings |
|-------------------------|---|--|---|
| Quan Luna et al. (2011) | Flow depth, h Impact pressure, p | Logistic | $V = \frac{1.49 \times (h / 2.51)^{1.938}}{1 + (h / 2.51)^{1.938}}$ $V = \frac{1.59 \times (p / 28.16)^{1.808}}{1 + (p / 28.16)^{1.808}}$ |
| Eidsvig et al. (2014) | Flow depth, h | Weibull distribution | $V = 1 - e^{-0.27h^{2.97}}$ |
| Kang and Kim (2016) | Flow depth, h Flow velocity, v Impact pressure, p | Sigmoid, S-shaped | $V = 1 - e^{-0.170h^{1.537}}$ $V = 1 - e^{-0.009v^{2.775}}$ $V = 1 - e^{-0.005p^{1.690}}$ |
| Zhang et al. (2018) | Flow depth, h Flow velocity, v Impact pressure, p Momentum flux, f Overturning moment, m Relative burial height, b | Logistic | $V = \frac{0.12 \times h^{3.39}}{1 + 9.24h^{3.39}} V = \frac{0.17 \times v^{2.45}}{1 + 6.54 \times v^{2.45}}$ $V = \frac{0.08 \times p^{1.08}}{1 + 15.45p^{1.08}} V = \frac{0.24 \times f^{0.40}}{1 + 10.23 \times f^{0.40}}$ $V = \frac{0.15 \times m^{1.15}}{1 + 7.83m^{1.15}} V = \frac{1096 \times b^{1.54}}{1 + 0.0009b^{1.54}}$ |
| Chen et al. (2021) | Momentum flux, f | Exponential | $V = 1 / (1 + e^{-1.036f + 4.721})$ |
| Wang et al. (2024) | Flow depth, h Impact pressure, p | Weibull distribution | $V = 1 - e^{-0.53h^{3.26}}$ $V = 1 - e^{-0.49(0.1p)^{2.65}}$ |
| Lee et al. (2024) | Impact pressure, p | Avrami | $V = 1.129(1 - e^{-0.007 \times p^{1.530}})$ |
| This study | Flow depth, h Flow velocity, v Impact pressure, p Momentum flux, f Overturning moment, m Relative burial height, b | Lognormal cumulative distribution function | $V = \Phi \left[\frac{1}{0.60} \ln \left(\frac{h}{e^{0.44}} \right) \right] V = \Phi \left[\frac{1}{1.05} \ln \left(\frac{v}{e^{-0.69}} \right) \right]$ $V = \Phi \left[\frac{1}{0.66} \ln \left(\frac{p}{e^{2.26}} \right) \right] V = \Phi \left[\frac{1}{2.61} \ln \left(\frac{f}{e^{-0.87}} \right) \right]$ $V = \Phi \left[\frac{1}{1.58} \ln \left(\frac{m}{e^{-0.18}} \right) \right] V = \Phi \left[\frac{1}{0.67} \ln \left(\frac{b}{e^{-1.37}} \right) \right]$ |



568

569

570

571 Figure 14. Comparison of the vulnerability curves with previous models for different debris
 572 flow intensities.

573 Finally, the differences between the various vulnerability curves also depend on the

574 vulnerability function models employed. Table 7 provides the existing vulnerability function
575 models, including Logistic, Weibull, Exponential, LNCDF and Avrami functions (Quan Luna
576 et al., 2011; Eidsvig et al., 2014; Kang and Kim, 2016; Zhang et al., 2018; Chen et al., 2021;
577 Luo et al., 2023; Wang et al., 2024; Lee et al., 2024). We analysed the performance of the
578 function models using data from this study and previous research (Fig. 15). The performance
579 values of different function models were compared using the flow depth and impact pressure
580 as examples (Fig. 15). The S-shaped function models (Logical, Weibull, Avrami and LNCDF
581 models) clearly performed better than the exponential function model did, whose vulnerability
582 curve did not pass through the origin (Fig. 15a; b) and may be heavily affected by outliers. In
583 addition, the coefficients of determination of all the function models did not significantly differ,
584 with R^2 values exceeding 0.88 (Table 7). This finding indicates that the coefficient of
585 determination only focuses on the degree of fit of the regression equation (Lee et al., 2023), but
586 it is not necessarily better for models with relatively large R^2 values, such as exponential
587 functions ($R^2=0.98$) with relatively large errors. The coefficient of determination is affected by
588 the complexity of the model, and overfitting may occur, which may lead to the model
589 performing well for training data but exhibiting a poor prediction ability with new data.
590 Therefore, the relative error and prediction accuracy of function models should be accounted
591 for (Wang et al., 2018).

592 Table 7 Performance comparison between various data-driven building vulnerability function
593 models

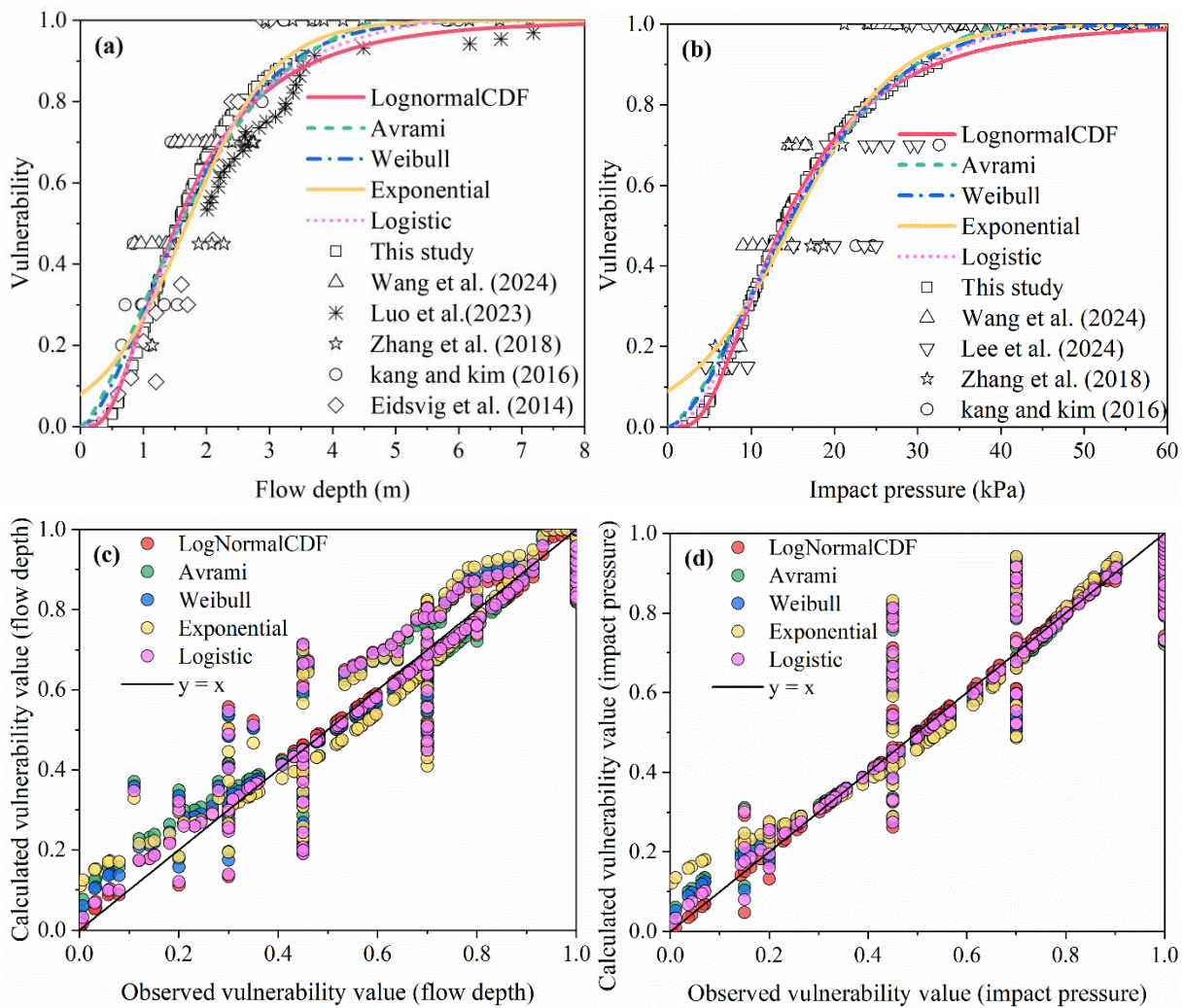
| Research ers | Vulnerab ility | Function models | Flow depth | | | | Impact pressure | | | |
|-----------------|-------------------|--------------------|------------|-----|-----|-----|-----------------|-----|-----|-----|
| | | | R^2 | MRE | TIC | PAF | R^2 | MRE | TIC | PAF |

| | models | | | | | | | | | |
|--|-------------|--|------|------|------|------|------|------|------|------|
| Quan Luna et al. (2011); Zhang et al. (2018) | Logistic | $V = \frac{a \times (\frac{x}{b})^c}{1 + (\frac{x}{b})^c}$ | 0.98 | 0.22 | 0.06 | 1.17 | 0.89 | 0.16 | 0.06 | 1.13 |
| Chen et al. (2021) | Exponential | $V = \frac{1}{1 + e^{ax+b}}$ | 0.98 | 0.76 | 0.06 | 1.23 | 0.88 | 0.48 | 0.07 | 1.19 |
| Eidsvig et al. (2014); Kang and Kim (2016); Wang et al. (2024) | Weibull | $V = 1 - e^{-(x/a)^b}$ | 0.88 | 0.37 | 0.06 | 1.20 | 0.89 | 0.22 | 0.06 | 1.15 |
| Lee et al. (2024) | Avrami | $V = a(1 - e^{-bx^c})$ | 0.99 | 0.45 | 0.06 | 1.21 | 0.89 | 0.24 | 0.06 | 1.16 |
| Luo et al. (2023); This study | LNCDF | $V = \Phi \left[\frac{1}{\beta} \ln \left(\frac{I}{I_m} \right) \right]$ | 0.88 | 0.16 | 0.06 | 1.15 | 0.88 | 0.09 | 0.06 | 1.09 |

594 Note: The parameters a, b, and c can be obtained directly by curve fitting.

595 In the comparison of the calculated and observed values, both the exponential and Avrami
596 functions clearly exhibited significant errors (Fig. 15c; d). Specifically, the MRE values for the
597 flow depth were 0.76 and 0.45, respectively, whereas the MRE values for the impact pressure
598 were 0.48 and 0.24, respectively (Table 7). However, the LNCDF model demonstrated the
599 highest statistical significance in terms of the relative error and accuracy, with MRE=0.16 and
600 PAF=1.15 for the flow depth and MRE=0.09 and PAF=1.09 for the impact pressure. In multiple
601 regression models, the coefficient of determination emphasizes the interpretability and fitting

602 performance, whereas the error prioritizes the prediction accuracy of the model. Overall, these
 603 two metrics provide complementary insights for evaluating the overall performance of the
 604 model. Overall, the performance of the various function models exhibited the following order:
 605 LNCDF > logistic > Weibull > Avrami > exponential models. LNCDF-based models are
 606 insensitive to single data points because of the statistical parameter curve fitting process for
 607 developing these models. It has been demonstrated that the LNCDF model can efficiently
 608 increase the prediction performance, leading to a substantial reduction in output uncertainty,
 609 and this model is recommended for future applications (Kean et al., 2019; Luo et al., 2023).

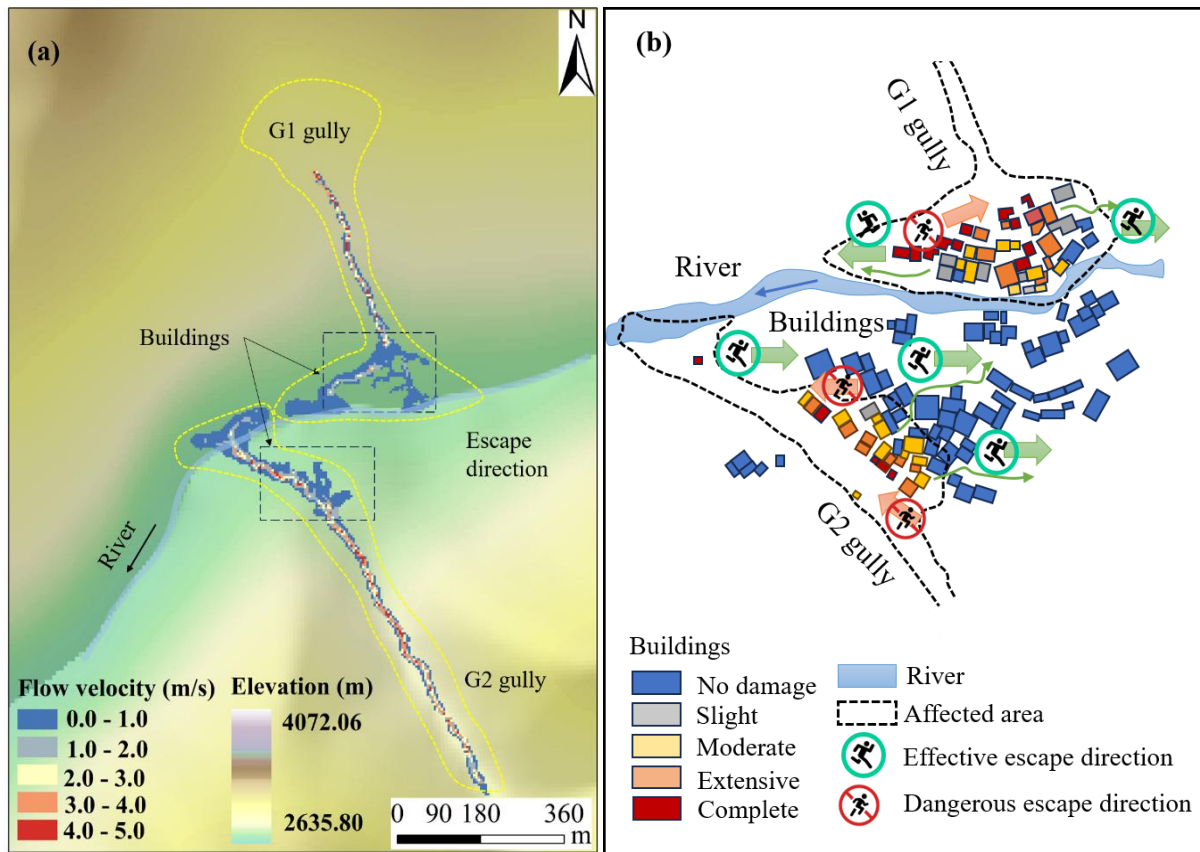


611
 612 Figure 15. Performance comparison between different vulnerability function models: (a) Flow

613 depth vulnerability models; (b) impact pressure vulnerability models; (c) observation and
614 calculation values of flow depth; (d) observation and calculation values of impact pressure.

615 **4.2 Disaster reduction and emergency response suggestions**

616 Both sides of Kule village are at risk of being impacted by the G1 and G2 gullies (Fig. 16).
617 Owing to the impact of wildfires, there is a large amount of loose material in these gullies,
618 which can trigger postfire debris flows again under low rainfall thresholds. Through the above
619 field investigations and simulation predictions, debris flows can seriously damage buildings
620 downstream of the alluvial fan and even block the Kule River, posing a severe threat to the lives
621 of more than 300 people in the village. The most dangerous situation occurs when debris flows
622 occur in the two gullies simultaneously (Fig. 16a). An immediate emergency response is crucial,
623 and the escape route should be oriented along the vertical direction of the debris flow channel
624 for reaching a safe location in high terrain (Fig. 16b). Left-bank residents should evacuate from
625 both sides, thereby avoiding crossing the river. In contrast, right-bank residents should evacuate
626 swiftly from the high-terrain area on their side. The safest suggestion is for residents to leave
627 the village under feasible conditions. In the long term, reforestation can stabilize soil and reduce
628 sediment into channels (Yang et al., 2022; Vahedifard et al., 2024). Thus, restoring vegetation
629 in burned areas is essential for effectively suppressing postfire debris flows and promoting local
630 ecological recovery (Yang et al., 2024).



631
 632 Figure 16. Disaster prediction and emergency response suggestions: (a) Simulation of debris
 633 flows occurring simultaneously in the G1 and G2 gullies; (b) emergency response and risk
 634 avoidance suggestions for the residents of Kule village.

635 4.3 Limitations and future work

636 Our results provide insights into assessing the vulnerability of buildings to debris flows
 637 triggered by wildfires in Yajiang County. A combination of numerical simulation and function
 638 model methods provided a distinct advantage in the development of vulnerability curves. The
 639 spatial distributions of the flow depth and flow velocity can be visualized, and detailed physical
 640 information can be obtained in a specific area (Zhang et al., 2018). Additionally, this study
 641 highlights the importance of acknowledging and addressing the inherent uncertainty associated
 642 with various debris flow intensity indicators and function models applied in vulnerability

643 assessments via a comparison of existing intensity indicators and evaluating the performance
644 of various function models. Notably, while the methodological framework combining field
645 investigation, numerical simulation, and vulnerability analysis is transferable to non-fire areas,
646 the specific vulnerability curve parameter values require recalibration when applied elsewhere.

647 However, several limitations should be acknowledged. First, during the numerical
648 modelling phase, terrain changes and sediment volume variations caused by debris flow
649 entrainment were neglected (Wang et al., 2024), and validation focused on depositional area
650 and runout volume, neglecting flow velocity along the path (Chen et al., 2021). Additionally,
651 due to limited understanding of postfire debris flow triggering and runoff mechanisms (Rengers
652 et al., 2016; Ouyang et al., 2023) and the introduction of burned wood into channels (Rengers
653 et al., 2023), only volume and peak flow were considered as recurrence period indicators (Cui
654 et al., 2018; Gorr et al., 2024), while other geological variables (e.g., particle size distribution,
655 viscosity, water content) were not incorporated (Chen et al., 2021). Second, differences in the
656 vulnerability curves of different indicators could cause uncertainty in vulnerability assessments
657 (Luo et al., 2023), where the percentage of buildings categorized may be inconsistent. The
658 slopes of the LNCDF-based curves increase slowly during the latter half, and intensity
659 calculations based on maximum values may lead to overestimation of ultimate failure strength
660 compared to actual values (Chen et al., 2021). Owing to the limited number of data points, to
661 increase the reliability of the vulnerability curves (Lee et al., 2024; Ettinger et al., 2016), more
662 data on postfire debris flow events and validations are needed in the future. Additionally,
663 transferring the G1-calibrated parameters to G2, an approach based on field observations of

664 comparable conditions between the adjacent catchments, introduces uncertainty as G2 is
665 potentially hazardous but has not yet experienced a debris flow. The G2 simulation results show
666 consistent orders of magnitude with similar regional events data (He et al., 2024). Direct
667 validation of G2 predictions warrants attention in future work. Finally, this study focused on
668 BC buildings, not accounting for other structural types (e.g., reinforced concrete frame
669 buildings), mechanical failure criteria for unreinforced masonry walls (Si et al., 2022), or
670 building-specific factors such as shape, orientation, number of floors, masking effects of
671 building complexes and construction codes (Lee et al., 2024; Wang et al., 2024). These
672 limitations emphasize the need for further research to enhance the comprehensive management
673 of hazard risks in mountainous rural areas.

674 Future research should focus on ensuring continuous, standardized post-event data
675 collection processes, which will enhance the practical applicability of the developed
676 vulnerability curves. Ultimately, this framework represents an important step towards
677 developing physical vulnerability models, thereby providing comprehensive insights into the
678 potential effects of future postfire debris flow events on buildings in similar regions and offering
679 valuable guidance for formulating disaster management and mitigation strategies.

680 **5. Conclusions**

681 This study assessed the vulnerability of buildings to postfire debris flows in Kule village,
682 Yajiang County. A physical vulnerability model for BC buildings was established to support
683 effective disaster management and emergency evacuation strategies for the region. The
684 conclusions are as follows:

685 (1) Field investigations characterized postfire debris flow features in the G1 and G2 gullies
686 and documented damage to 36 BC buildings in Kule village. The volume and peak discharge
687 of postfire debris flows were calculated, and the damage degree of buildings was categorized
688 using a range of vulnerability indices.

689 (2) Dynamic runout processes were simulated using the FLO-2D numerical model, with
690 the reconstructed results calibrated to ensure consistency with actual situations. The simulations
691 captured the debris flow intensities, including the flow depth, flow velocity, impact pressure,
692 momentum flux, overturning moment, and relative burial height.

693 (3) Physical vulnerability curves for BC buildings damaged by postfire debris flows in the
694 G1 gully were developed. The vulnerability model was subsequently applied to the G2 gully,
695 to predict potential building damage scenarios and their spatial distributions, enabling
696 emergency evacuation recommendations for Kule village in the event of simultaneous debris
697 flows in both gullies.

698 (4) Comparisons of different vulnerability curves, intensity indicators, and function
699 models revealed that momentum flux was the most sensitive indicator for distinguishing
700 damage categories, while impact pressure could provide more accurate vulnerability values.
701 Among the function models, the LNCDF function model demonstrated the highest statistical
702 performance (MRE=0.09, PAF=1.09).

703 (5) The proposed vulnerability model exhibits certain limitations, emphasizing the
704 importance of acknowledging and addressing the inherent uncertainty associated with various
705 intensity indicators, function models, triggering and runoff mechanisms underlying postfire

706 debris flows, and building structure and orientation in future research.

707 **Author contributions**

708 **JW:** Writing - original draft, Methodology, Validation, Conceptualization. **JC:** Writing -
709 Review & editing, Supervision, Funding acquisition. **LZ:** Investigation, Data curation. **FY:**
710 Software. **XL:** Investigation. **WZ:** Resources. **HC:** Formal analysis.

711 **Declaration of competing interest**

712 The authors have no conflicts of interest to declare.

713 **Acknowledgements**

714 This study was supported by the National Key R&D Program of China (Grant No.
715 2024YFC3012705), the Nyingchi National Sustainable Development Experimental Zone
716 Project (2023-SYQ-007), the National Natural Science Foundation of China (Grant No.
717 41925030) and the Science and Technology Research Program of the Institute of Mountain
718 Hazards and Environment, Chinese Academy of Sciences (Grant No. IMHE-ZDRW-02).

719 **Data availability**

720 The authors agree to make data supporting the results or analyses presented in this paper
721 available upon reasonable request to the first author and corresponding author.

722

Appendix A Debris flow intensities and building damage degree in G1 gully

| NO. | Flow depth (m) | Flow velocity (m/s) | Impact pressure (kPa) | Momentum flux (m^3/s^2) | Overturning moment (m^2/s) | Relative burial height | Damage degree |
|-----|----------------|---------------------|-----------------------|---|--|------------------------|---------------|
| 1 | 2.00 | 1.69 | 21.52 | 5.71 | 3.38 | 0.71 | Complete |
| 2 | 0.51 | 0.31 | 4.41 | 0.05 | 0.16 | 0.08 | Slight |
| 3 | 2.91 | 1.52 | 28.17 | 6.72 | 4.42 | 0.49 | Complete |
| 4 | 1.61 | 0.50 | 13.84 | 0.40 | 0.81 | 0.32 | Extensive |
| 5 | 1.98 | 1.05 | 18.37 | 2.18 | 2.08 | 0.36 | Extensive |
| 6 | 0.81 | 0.13 | 6.78 | 0.01 | 0.11 | 0.12 | Slight |
| 7 | 1.94 | 0.68 | 16.95 | 0.90 | 1.32 | 0.37 | Extensive |
| 8 | 1.61 | 0.85 | 14.64 | 1.16 | 1.37 | 0.27 | Extensive |
| 9 | 1.40 | 0.38 | 11.91 | 0.20 | 0.53 | 0.23 | Moderate |
| 10 | 2.20 | 1.35 | 21.42 | 4.01 | 2.97 | 0.29 | Complete |
| 11 | 1.51 | 0.87 | 13.87 | 1.14 | 1.31 | 0.30 | Extensive |
| 12 | 2.03 | 1.93 | 23.24 | 7.56 | 3.92 | 0.47 | Complete |
| 13 | 1.02 | 0.50 | 8.92 | 0.26 | 0.51 | 0.15 | Moderate |
| 14 | 1.21 | 0.44 | 10.41 | 0.23 | 0.53 | 0.18 | Moderate |
| 15 | 2.06 | 1.55 | 21.24 | 4.95 | 3.19 | 0.52 | Complete |
| 16 | 1.72 | 0.50 | 14.75 | 0.43 | 0.86 | 0.34 | Extensive |
| 17 | 2.08 | 1.32 | 20.29 | 3.62 | 2.75 | 0.42 | Complete |
| 18 | 0.61 | 0.19 | 5.14 | 0.02 | 0.12 | 0.12 | Slight |
| 19 | 1.25 | 0.48 | 10.80 | 0.29 | 0.60 | 0.21 | Moderate |
| 20 | 1.59 | 0.57 | 13.80 | 0.52 | 0.91 | 0.32 | Extensive |
| 21 | 0.83 | 0.39 | 7.17 | 0.13 | 0.32 | 0.18 | Moderate |
| 22 | 0.25 | 0.28 | 2.22 | 0.02 | 0.07 | 0.04 | Slight |
| 23 | 2.02 | 1.61 | 21.23 | 5.24 | 3.25 | 0.37 | Complete |
| 24 | 1.61 | 1.08 | 15.39 | 1.88 | 1.74 | 0.24 | Extensive |
| 25 | 1.24 | 0.42 | 10.63 | 0.22 | 0.52 | 0.18 | Moderate |
| 26 | 1.91 | 1.21 | 18.40 | 2.80 | 2.31 | 0.29 | Extensive |
| 27 | 1.17 | 0.37 | 9.98 | 0.16 | 0.43 | 0.15 | Moderate |
| 28 | 0.50 | 0.04 | 4.17 | 0.00 | 0.02 | 0.06 | Slight |
| 29 | 0.61 | 0.21 | 5.16 | 0.03 | 0.13 | 0.08 | Slight |
| 30 | 2.41 | 1.93 | 26.41 | 8.98 | 4.65 | 0.40 | Complete |
| 31 | 2.28 | 1.75 | 24.20 | 6.98 | 3.99 | 0.41 | Complete |
| 32 | 0.60 | 0.02 | 5.00 | 0.00 | 0.01 | 0.09 | Slight |
| 33 | 2.54 | 1.25 | 23.81 | 3.97 | 3.18 | 0.46 | Complete |
| 34 | 2.61 | 1.24 | 24.36 | 4.01 | 3.24 | 0.44 | Complete |
| 35 | 2.38 | 1.90 | 25.96 | 8.59 | 4.52 | 0.38 | Complete |
| 36 | 0.35 | 0.18 | 2.97 | 0.01 | 0.06 | 0.10 | Slight |

724 **Appendix B Debris flow intensities and predicted building counts in G2**

725 **gully: (a) Design frequency P=1%; (b) Design frequency P=2%**

726 (a) Design frequency P=1%

| NO. | Flow depth (m) | Flow velocity (m/s) | Impact pressure (kPa) | Momentum flux (m ³ /s ²) | Overturning moment (m ² /s) | Relative burial height | Damage degree |
|-----|----------------|---------------------|-----------------------|---|--|------------------------|---------------|
| 1 | 2.30 | 0.69 | 19.97 | 1.10 | 1.59 | 0.38 | Extensive |
| 2 | 1.79 | 0.31 | 15.07 | 0.17 | 0.55 | 0.29 | Moderate |
| 3 | 1.90 | 0.67 | 16.59 | 0.85 | 1.27 | 0.42 | Extensive |
| 4 | 1.77 | 0.31 | 14.91 | 0.17 | 0.55 | 0.30 | Moderate |
| 5 | 1.15 | 0.50 | 10.00 | 0.29 | 0.58 | 0.21 | Moderate |
| 6 | 1.69 | 0.24 | 14.18 | 0.10 | 0.41 | 0.26 | Moderate |
| 7 | 2.54 | 0.67 | 21.92 | 1.14 | 1.70 | 0.39 | Extensive |
| 8 | 2.50 | 0.68 | 21.61 | 1.16 | 1.70 | 0.42 | Extensive |
| 9 | 3.50 | 2.00 | 35.96 | 14.00 | 7.00 | 0.58 | Complete |
| 10 | 3.10 | 1.80 | 31.33 | 10.04 | 5.58 | 0.69 | Complete |
| 11 | 2.96 | 1.18 | 27.02 | 4.12 | 3.49 | 0.66 | Complete |
| 12 | 1.60 | 0.50 | 13.75 | 0.40 | 0.80 | 0.21 | Moderate |
| 13 | 2.50 | 1.12 | 22.96 | 3.14 | 2.80 | 0.42 | Extensive |
| 14 | 2.00 | 0.80 | 17.75 | 1.28 | 1.60 | 0.44 | Extensive |
| 15 | 1.70 | 0.32 | 14.34 | 0.17 | 0.54 | 0.28 | Moderate |
| 16 | 1.51 | 0.29 | 12.72 | 0.13 | 0.44 | 0.23 | Moderate |
| 17 | 1.00 | 0.20 | 8.40 | 0.04 | 0.20 | 0.14 | Slight |
| 18 | 2.23 | 1.10 | 20.63 | 2.70 | 2.45 | 0.45 | Extensive |
| 19 | 1.44 | 0.65 | 12.71 | 0.61 | 0.94 | 0.29 | Moderate |
| 20 | 3.27 | 2.36 | 36.71 | 18.21 | 7.72 | 0.65 | Complete |
| 21 | 2.50 | 0.95 | 22.36 | 2.26 | 2.38 | 0.42 | Extensive |
| 22 | 1.78 | 0.45 | 15.17 | 0.36 | 0.80 | 0.30 | Moderate |
| 23 | 3.15 | 1.60 | 30.59 | 8.06 | 5.04 | 0.70 | Complete |
| 24 | 1.21 | 0.40 | 10.35 | 0.19 | 0.48 | 0.20 | Moderate |

727

728 (b) Design frequency P=2%

| NO. | Flow depth (m) | Flow velocity (m/s) | Impact pressure (kPa) | Momentum flux (m ³ /s ²) | Overturning moment (m ² /s) | Relative burial height | Damage degree |
|-----|----------------|---------------------|-----------------------|---|--|------------------------|---------------|
| 1 | 1.70 | 0.44 | 14.49 | 0.33 | 0.75 | 0.28 | Moderate |
| 2 | 1.72 | 0.30 | 14.48 | 0.15 | 0.52 | 0.28 | Moderate |
| 3 | 1.35 | 0.31 | 11.41 | 0.13 | 0.42 | 0.30 | Moderate |
| 4 | 1.76 | 0.30 | 14.81 | 0.16 | 0.53 | 0.29 | Moderate |
| 5 | 0.90 | 0.20 | 7.57 | 0.04 | 0.18 | 0.16 | Slight |
| 6 | 1.62 | 0.33 | 13.68 | 0.18 | 0.53 | 0.25 | Moderate |
| 7 | 2.40 | 0.66 | 20.73 | 1.05 | 1.58 | 0.37 | Extensive |
| 8 | 1.80 | 0.45 | 15.34 | 0.36 | 0.81 | 0.30 | Moderate |
| 9 | 2.90 | 1.88 | 30.17 | 10.25 | 5.45 | 0.48 | Complete |
| 10 | 2.00 | 0.84 | 17.86 | 1.41 | 1.68 | 0.44 | Extensive |
| 11 | 2.75 | 1.25 | 25.56 | 4.30 | 3.44 | 0.61 | Complete |
| 12 | 1.07 | 0.30 | 9.07 | 0.10 | 0.32 | 0.14 | Slight |
| 13 | 2.45 | 0.95 | 21.94 | 2.21 | 2.33 | 0.41 | Extensive |
| 14 | 1.15 | 0.32 | 9.75 | 0.12 | 0.37 | 0.26 | Moderate |
| 15 | 1.50 | 0.38 | 12.74 | 0.22 | 0.57 | 0.25 | Moderate |
| 16 | 1.44 | 0.30 | 12.15 | 0.13 | 0.43 | 0.22 | Moderate |
| 17 | 1.22 | 0.11 | 10.18 | 0.01 | 0.13 | 0.17 | Slight |
| 18 | 1.50 | 0.50 | 12.92 | 0.38 | 0.75 | 0.30 | Moderate |
| 19 | 1.40 | 0.49 | 12.07 | 0.34 | 0.69 | 0.28 | Moderate |
| 20 | 2.80 | 2.30 | 32.32 | 14.81 | 6.44 | 0.56 | Complete |
| 21 | 2.34 | 0.85 | 20.72 | 1.69 | 1.99 | 0.39 | Extensive |
| 22 | 1.70 | 0.45 | 14.51 | 0.34 | 0.77 | 0.28 | Moderate |
| 23 | 3.00 | 1.30 | 27.86 | 5.07 | 3.90 | 0.67 | Complete |
| 24 | 1.00 | 0.30 | 8.48 | 0.09 | 0.30 | 0.17 | Slight |

729

730 **References**

- 731 Barnhart, K. R., Miller, C. R., Rengers, F. K., & Kean, J. W. (2024). Evaluation of debris-flow
732 building damage forecasts. *Natural Hazards and Earth System Sciences*, 24(4), 1459-1483.
733 <https://doi.org/10.5194/nhess-24-1459-2024>
- 734 Chang, M., Liu, Y., Zhou, C., & Che, H. (2020). Hazard assessment of a catastrophic mine
735 waste debris flow of Hou Gully, Shimian, China. *Engineering Geology*, 275, 105733.
736 <https://doi.org/10.1016/j.enggeo.2020.105733>
- 737 Chen, M., Tang, C., Zhang, X., Xiong, J., Chang, M., Shi, Q., ... & Li, M. (2021). Quantitative
738 assessment of physical fragility of buildings to the debris flow on 20 August 2019 in the
739 Cutou gully, Wenchuan, southwestern China. *Engineering Geology*, 293, 106319.
740 <https://doi.org/10.1016/j.enggeo.2021.106319>
- 741 Cui, P., Guo, X., Yan, Y., Li, Y., & Ge, Y. (2018). Real-time observation of an active debris flow
742 watershed in the Wenchuan Earthquake area. *Geomorphology*, 321, 153-166.
743 <https://doi.org/10.1016/j.geomorph.2018.08.024>
- 744 Cui, P., Hu, K., Zhuang, J., Yang, Y., & Zhang, J. (2011). Prediction of debris-flow danger area
745 by combining hydrological and inundation simulation methods. *Journal of Mountain
746 Science*, 8, 1-9. <https://doi.org/10.1007/s11629-011-2040-8>
- 747 Cui, W. R., Chen, J. G., Chen, X. Q., Tang, J. B., & Jin, K. (2023). Debris flow characteristics
748 of the compound channels with vegetated floodplains. *Science of The Total Environment*,
749 868, 161586. <https://doi.org/10.1016/j.scitotenv.2023.161586>
- 750 Ding, X. Y., Hu, W. J., Liu, F., & Yang, X. (2023). Risk assessment of debris flow disaster in

751 mountainous area of northern Yunnan province based on FLO-2D under the influence of
752 extreme rainfall. *Frontiers in Environmental Science*, 11, 1252206.
753 <https://doi.org/10.3389/fenvs.2023.1252206>

754 Eidsvig, U. M. K., Papathoma-Köhle, M., Du, J., Glade, T., & Vangelsten, B. V. (2014).
755 Quantification of model uncertainty in debris flow vulnerability assessment. *Engineering*
756 *Geology*, 181, 15-26. <https://doi.org/10.1016/j.enggeo.2014.08.006>

757 Ettinger, S., Mounaud, L., Magill, C., Yao-Lafourcade, A. F., Thouret, J. C., Manville, V., ... &
758 Llerena, N. M. (2016). Building vulnerability to hydro-geomorphic hazards: Estimating
759 damage probability from qualitative vulnerability assessment using logistic regression.
760 *Journal of Hydrology*, 541, 563-581. <https://doi.org/10.1016/j.jhydrol.2015.04.017>

761 Fuchs, S., Heiss, K., & Hübl, J. J. N. H. (2007). Towards an empirical vulnerability function
762 for use in debris flow risk assessment. *Natural Hazards and Earth System Sciences*, 7(5),
763 495-506. <https://doi.org/10.5194/nhess-7-495-2007>

764 Fuchs, S., Keiler, M., Ortlepp, R., Schinke, R., & Papathoma-Köhle, M. (2019). Recent
765 advances in vulnerability assessment for the built environment exposed to torrential
766 hazards: Challenges and the way forward. *Journal of hydrology*, 575, 587-595.
767 <https://doi.org/10.1016/j.jhydrol.2019.05.067>

768 Gartner, J. E., Cannon, S. H., & Santi, P. M. (2014). Empirical models for predicting volumes
769 of sediment deposited by debris flows and sediment-laden floods in the transverse ranges
770 of southern California. *Engineering Geology*, 176, 45-56.
771 <https://doi.org/10.1016/j.enggeo.2014.04.008>

772 Gorr, A., McGuire, L., & Youberg, A. (2024). Empirical models for postfire debris-flow volume
773 in the southwest United States. *Journal of Geophysical Research: Earth Surface*, 129(11),
774 e2024JF007825. <https://doi.org/10.1029/2024jf007825>

775 Guo, X., Hürlimann, M., Cui, P., Chen, X., & Li, Y. (2024). Monitoring cases of rainfall-induced
776 debris flows in China. *Landslides*, 21(10), 2447-2466. [https://doi.org/10.1007/s10346-](https://doi.org/10.1007/s10346-024-02316-7)
777 [024-02316-7](https://doi.org/10.1007/s10346-024-02316-7)

778 He, K., Hu, X., Wu, Z., Zhong, Y., Zhou, Y., Gong, X., & Luo, G. (2024). Preliminary analysis
779 of the wildfire on March 15, 2024, and the following post-fire debris flows in Yajiang
780 County, Sichuan, China. *Landslides*, 21(12), 3179-3189. [https://doi.org/10.1007/s10346-](https://doi.org/10.1007/s10346-024-02364-z)
781 [024-02364-z](https://doi.org/10.1007/s10346-024-02364-z)

782 Hu, K. H., Cui, P., & Zhang, J. Q. (2012). Characteristics of damage to buildings by debris
783 flows on 7 August 2010 in Zhouqu, Western China. *Natural Hazards and Earth System*
784 *Sciences*, 12(7), 2209-2217. <https://doi.org/10.5194/nhess-12-2209-2012>

785 Jakob, M., Stein, D., & Ulmi, M. (2012). Vulnerability of buildings to debris flow impact.
786 *Natural hazards*, 60, 241-261. <https://doi.org/10.1007/s11069-011-0007-2>

787 Kang, H. S., & Kim, Y. T. (2016). The physical vulnerability of different types of building
788 structure to debris flow events. *Natural Hazards*, 80, 1475-1493.
789 <https://doi.org/10.1007/s11069-015-2032-z>

790 Kean, J. W., Staley, D. M., Lancaster, J. T., Rengers, F. K., Swanson, B. J., Coe, J. A., ... &
791 Lindsay, D. N. (2019). Inundation, flow dynamics, and damage in the 9 January 2018
792 Montecito debris-flow event, California, USA: Opportunities and challenges for post-

793 wildfire risk assessment. *Geosphere*, 15(4), 1140-1163.
794 <https://doi.org/10.1130/ges02048.1>

795 Lee, J. S., Song, C. H., Pradhan, A. M. S., Ha, Y. S., & Kim, Y. T. (2024). Development of
796 structural type-based physical vulnerability curves to debris flow using numerical analysis
797 and regression model. *International Journal of Disaster Risk Reduction*, 106, 104431.
798 <https://doi.org/10.1016/j.ijdr.2024.104431>

799 Luo, H. Y., Zhang, L. M., Zhang, L. L., He, J., & Yin, K. S. (2023). Vulnerability of buildings
800 to landslides: The state of the art and future needs. *Earth-Science Reviews*, 238, 104329.
801 <https://doi.org/10.1016/j.earscirev.2023.104329>

802 Luo, H., Zhang, L., Wang, H., & He, J. (2020). Multi-hazard vulnerability of buildings to debris
803 flows. *Engineering Geology*, 279, 105859. <https://doi.org/10.3389/feart.2022.827438>

804 Marchi L, Arattano M, Deganutti AM (2002) Ten years of debris-flow monitoring in the
805 Moscardo Torrent (Italian Alps). *Geomorphology* 46:1–17. [https://doi.org/10.1016/s0169-](https://doi.org/10.1016/s0169-555x(01)00162-3)
806 [555x\(01\)00162-3](https://doi.org/10.1016/s0169-555x(01)00162-3)

807 McGuire, L. A., Ebel, B. A., Rengers, F. K., Vieira, D. C., & Nyman, P. (2024). Fire effects on
808 geomorphic processes. *Nature Reviews Earth & Environment*, 1-18.
809 <https://doi.org/10.1038/s43017-024-00557-7>

810 Navratil, O., Liébault, F., Bellot, H., Travaglini, E., Theule, J., Chambon, G., & Laigle, D.
811 (2013). High-frequency monitoring of debris-flow propagation along the Réal Torrent,
812 Southern French Prealps. *Geomorphology*, 201, 157-171.
813 <https://doi.org/10.1016/j.geomorph.2013.06.017>

814 Ouyang, C., Wang, Z., An, H., Liu, X., & Wang, D. (2019). An example of a hazard and risk
815 assessment for debris flows—A case study of Niwan Gully, Wudu, China. *Engineering*
816 *Geology*, 263, 105351. <https://doi.org/10.1016/j.enggeo.2019.105351>

817 Ouyang, C., Xiang, W., An, H., Wang, F., Yang, W., & Fan, J. (2023). Mechanistic Analysis and
818 Numerical Simulation of the 2021 Post-Fire Debris Flow in Xiangjiao Catchment, China.
819 *Journal of Geophysical Research: Earth Surface*, 128(1), e2022JF006846.
820 <https://doi.org/10.1029/2022jf006846>

821 Papathoma-Köhle, M., Gems, B., Sturm, M., & Fuchs, S. (2017). Matrices, curves and
822 indicators: A review of approaches to assess physical vulnerability to debris flows. *Earth-*
823 *Science Reviews*, 171, 272-288. <https://doi.org/10.1016/j.earscirev.2017.06.007>

824 Papathoma-Köhle, M., Schlögl, M., Dosser, L., Roesch, F., Borga, M., Erlicher, M., ... & Fuchs,
825 S. (2022). Physical vulnerability to dynamic flooding: Vulnerability curves and
826 vulnerability indices. *Journal of Hydrology*, 607, 127501.
827 <https://doi.org/10.1016/j.jhydrol.2022.127501>

828 Quan Luna, B., Blahut, J., Van Westen, C. J., Sterlacchini, S., Van Asch, T., & Akbas, S. O.
829 (2011). The application of numerical debris flow modelling for the generation of physical
830 vulnerability curves. *Natural hazards and earth system sciences*, 11(7), 2047-2060.
831 <https://doi.org/10.5194/nhess-11-2047-2011>

832 Rengers, F. K., McGuire, L. A., Barnhart, K. R., Youberg, A. M., Cadol, D., Gorr, A. N., ... &
833 Kean, J. W. (2023). The influence of large woody debris on post-wildfire debris flow
834 sediment storage. *Natural Hazards and Earth System Sciences*, 23(6), 2075-2088.

835 <https://doi.org/10.5194/nhess-23-2075-2023>

836 Rengers, F. K., McGuire, L. A., Kean, J. W., Staley, D. M., & Hobley, D. E. J. (2016). Model
837 simulations of flood and debris flow timing in steep catchments after wildfire. *Water*
838 *Resources Research*, 52(8), 6041-6061. <https://doi.org/10.1002/2015wr018176>

839 Rickenmann D (1999) Empirical relationships for debris flows. *Nat Hazards* 19:47–77

840 Scheidl, C., & Rickenmann, D. (2010). Empirical prediction of debris-flow mobility and
841 deposition on fans. *Earth Surface Processes and Landforms: The Journal of the British*
842 *Geomorphological Research Group*, 35(2), 157-173. <https://doi.org/10.1002/esp.1897>

843 Si, G. W., Chen, X. Q., Chen, J. G., Zhao, W. Y., Li, S., & Li, X. N. (2022). Failure criteria of
844 unreinforced masonry walls of rural buildings under the impact of flash floods in
845 mountainous regions. *Journal of Mountain Science*, 19(12), 3388-3406.
846 <https://doi.org/10.1007/s11629-022-7491-6>

847 Sichuan Hydrological Manual (1984) Rainstorm-runoff calculation method in small watershed,
848 1984, Sichuan Water Conservancy and Power Department. Electronic publishing.

849 Thomas, M. A., Kean, J. W., McCoy, S. W., Lindsay, D. N., Kostelnik, J., Cavagnaro, D. B., ...
850 & Collins, B. D. (2023). Postfire hydrologic response along the Central California (USA)
851 coast: insights for the emergency assessment of postfire debris-flow hazards. *Landslides*,
852 20(11), 2421-2436. <https://doi.org/10.1007/s10346-023-02106-7>

853 Totschnig, R., Sedlacek, W., & Fuchs, S. (2011). A quantitative vulnerability function for fluvial
854 sediment transport. *Natural Hazards*, 58, 681-703.

855 Vahedifard, F., Abdollahi, M., Leshchinsky, B. A., Stark, T. D., Sadegh, M., & AghaKouchak,

856 A. (2024). Interdependencies between wildfire-induced alterations in soil properties, near-
857 surface processes, and geohazards. *Earth and Space Science*, 11(2), e2023EA003498.
858 <https://doi.org/10.1029/2023ea003498>

859 Wei, L., Hu, K., Liu, S., Ning, L., Zhang, X., Zhang, Q., & Rahim, M. A. (2024). The
860 vulnerability of buildings to a large-scale debris flow and outburst flood hazard cascade
861 that occurred on 30 August 2020 in Ganluo, southwest China. *Natural Hazards and Earth
862 System Sciences*, 24(11), 4179-4197. <https://doi.org/10.5194/nhess-24-4179-2024>

863 Wang, T., Chen, J., Chen, X., You, Y., & Cheng, N. (2018). Application of incomplete similarity
864 theory to the estimation of the mean velocity of debris flows. *Landslides*, 15, 2083-2091.
865 <https://doi.org/10.1007/s10346-018-1045-6>

866 Wang, T., Yin, K., Li, Y., Chen, L., Xiao, C., Zhu, H., & van Westen, C. (2024). Physical
867 vulnerability curve construction and quantitative risk assessment of a typhoon-triggered
868 debris flow via numerical simulation: A case study of Zhejiang Province, SE China.
869 *Landslides*, 21(6), 1333-1352. <https://doi.org/10.1007/s10346-024-02218-8>

870 Yang, Y., Hu, X., Han, M., He, K., Liu, B., Jin, T., ... & Huang, J. (2022). Post-fire temporal
871 trends in soil properties and revegetation: Insights from different wildfire severities in the
872 Hengduan Mountains, Southwestern China. *Catena*, 213, 106160.
873 <https://doi.org/10.1016/j.catena.2022.106160>

874 Yang, H., Liu, J., Sun, H., You, Y., Zhao, W., & Yang, D. (2024). Evolution characteristics of
875 post-fire debris flow in Xiangjiao gully, Muli County. *Catena*, 246, 108353.
876 <https://doi.org/10.1016/j.catena.2024.108353>

- 877 Zhang, B., Zhang, G., Fang, H., Wu, S., & Li, C. (2024). Risk assessment of flash flood under
878 climate and land use and land cover change in Tianshan Mountains, China. *International*
879 *Journal of Disaster Risk Reduction*, 115, 105019.
880 <https://doi.org/10.1016/j.ijdrr.2024.105019>
- 881 Zhang, S., Zhang, L., Li, X., & Xu, Q. (2018). Physical vulnerability models for assessing
882 building damage by debris flows. *Engineering Geology*, 247, 145-158.
883 <https://doi.org/10.1016/j.enggeo.2018.10.017>
- 884 Zhou, B.F., Li, D.J., Luo, D.F., Lv, R.R., Yang, Q.X., 1991. *Guide to Prevention of Debris Flow*.
885 Beijing, China.
- 886 Zhang, W., Chen, J., Ma, J., Cao, C., Yin, H., Wang, J., & Han, B. (2023). Evolution of sediment
887 after a decade of the Wenchuan earthquake: a case study in a protected debris flow
888 catchment in Wenchuan County, China. *Acta Geotechnica*, 18(7), 3905-3926.
889 <https://doi.org/10.1007/s11440-022-01789-x>